
MODELLING OF FUNCTIONALLY GRADED TRIPLY PERIODIC MINIMAL SURFACE (FG-TPMS) PLATES

A PREPRINT

✉ **H. Nguyen-Xuan***
CIRTECH Institute
HUTECH University
Ho Chi Minh City, Viet Nam
ngx.hung@hutech.edu.vn

✉ **Kim Q. Tran**
CIRTECH Institute
HUTECH University
Ho Chi Minh City, Viet Nam
tqkim.work@gmail.com

✉ **Chien H. Thai**
Division of Computational Mechanics
Institute for Computational Sciences
Ton Duc Thang University
Ho Chi Minh City, Viet Nam

✉ **Jaehong Lee**
Deep Learning Architecture Research Center
Sejong University
209 Neungdong Ro, Gwangjin Ku, Seoul 05006, Korea
jhlee@sejong.ac.kr

March 27, 2023

ABSTRACT

Functionally graded porous plates have been validated as remarkable lightweight structures with excellent mechanical characteristics and numerous applications. With inspiration from the high strength-to-volume ratio of triply periodic minimal surface (TPMS) structures, a new model of porous plates, which is called a functionally graded TPMS (FG-TPMS) plate, is investigated in this paper. Three TPMS architectures including Primitive (P), Gyroid (G), and wrapped package-graph (IWP) with different graded functions are presented. To predict the mechanical responses, a new fitting technique based on a two-phase piece-wise function is employed to evaluate the effective moduli of TPMS structures, including elastic modulus, shear modulus, and bulk modulus. In addition, this function corresponds to the cellular structure formulation in the context of relative density. The separated phases of the function are divided by the different deformation behaviors. Furthermore, another crucial mechanical property of porous structure, i.e. Poisson's ratio, is also achieved by a similar fitting technique. To verify the mechanical characteristics of the FG-TPMS plate, the generalized displacement field is modeled by a seventh-order shear deformation theory (SeSDT). A NURBS-based isogeometric analysis (IGA) is then employed to capture the C^1 continuity in approximations. Numerical examples regarding static, buckling, and free vibration analyses of FG-TPMS plates are illustrated to confirm the reliability and accuracy of the proposed approach. Consequently, these FG-TPMS structures can provide much higher stiffness than the same-weight isotropic plate. The greater stiffness-to-weight ratio of these porous plates compared to the full-weight isotropic ones should be considered the most remarkable feature. Thus, these complex porous structures have numerous practical applications because of these high ratios and their fabrication ability through additive manufacturing (AM) technology.

Keywords Cellular materials · triply periodic minimal surface · higher order shear deformation theory · non-uniform rational B-splines (NURBS) · isogeometric analysis

*Corresponding author.

1 Introduction

Biomimicry structure has been known as a robust group of nature-inspired structures. Its applications could be found in various engineering fields such as civil construction, biomedical engineering, crash-worthiness and aerospace material, etc [1]. Thanks to the development of additive manufacturing (AM) or 3D printing, numerous sophisticated structures could be fabricated precisely. For instance, a group of nature-inspired structures which consists of zero mean curvature surfaces so-called TPMS structure has been manufactured by 3D printing technology. Recently, several solid-type cellular structures have been developed to apply these complex geometries including skeletal-based, network-based, thicken-based, and sheet-based structures. The latter is suggested to have higher mechanical performances than other solid types in view of thermal, electrical conductivity, and mechanical properties [2]. Studies on this structure type have been conducted using the finite element method (FEM) and experiments. An overview of several related studies can be found in [3].

Furthermore, wide-range applications of sheet-based TPMS structures have been reported in recent studies. From the prospect of energy absorption, investigations on protection system strategies might be noticed. For instance, plastic TPMSs have been discovered in the spatial transportation field [4]. Stainless steel materials have also been utilized to fabricate and assess the energy-absorbing capacity of sheet-based Primitive, Gyroid, and Diamond structures [5]. Another report by Liang *et al.* [6] has conducted biaxial and triaxial compression tests on Gyroid blocks to investigate the energy aspects of porous materials. In addition, the sound absorption properties of these structures were also determined in the study by Yang *et al.* [7]. Recently, the sandwich panels with TPMS cores have been conducted to specify their sound insulation effect with the thin plate model theory [8]. In a biomechanics view, the low relative density of TPMS should be used to mimic the human bone joints [9] or even the bone replacements based on the great strength-to-weight ratio and the controllable pore size characteristic [10]. Several applications of TPMS as sandwich plates were reviewed, in which the Gyroid structure exhibited a strong influence on both impact and explosive resistances [11]. The semi-theoretical approach was adopted to verify the numerical results of Primitive, Neovius, and IWP sandwich beams [12]. Moreover, TPMS reinforcement strategies have been recently found to be an interesting research area. Researchers have verified the enhancement in bending behaviors of cementitious beams reinforced with plastic 3D printed Primitive TPMS cores subjected to both static [13] and dynamic loads [14]. Dang-Bao *et al.* [15] proposed a new cement breakwater solution for the improved hydrodynamic responses of Gyroid-TPMS structures.

In another aspect of understanding TPMS structures, tunable properties (i.e. pore size, anisotropic index, Poisson's ratio, plastic deformation, etc) can be accomplished by modifying the implicit geometry function. The functional grading and hybridizing relative density might also change these properties. Karuna *et al.* [16] studied the fluid properties of various modified geometries of IWP structures. However, diverge schemes of TPMS anisotropy are probably difficult to be applied. For that reason, an isotropic design based on the optimization of hollow structures has been operated [17]. Furthermore, negative Poisson's ratios of sheet-based Primitive and Gyroid composites were discovered by Chawla *et al.* [18]. With different functionally grading strategies, the mechanical properties and the deformation mechanism of Primitive TPMS can be simply controlled for specific purposes [19].

Despite a large amount of researches on these TPMS structures, there are possibly only a few reports on the functionally graded TPMS structures. For a specific case, buckling and free vibration behaviors of FG-TPMS beams were pointed out in [20]. In the following study, the flexural properties of several FG-TPMS and hybrid TPMS beams were experimentally and numerically explored by Egeh *et al.* [21]. However, the FG-TPMS plate should be considered an improved structure in the aspects of mechanical properties and fabrication ability. In a relevant work, a bio-inspired functionally graded Gyroid sandwich panel [22] exhibited its effectiveness in blast resistance. Furthermore, to address the potential application of FG-TPMS plate structures, popular plate theories consisting of the classical thin plate theory (CPT), the first-order shear deformation theory (FSDT), and the higher-order shear deformation theory (HSDT) can be utilized for modelling of FG-TPMS plates. It was shown that all these theories could be unified by a common polynomial form [23]. In addition, a high-order shear deformation theory [24] with three variables (THSDT) is suitable for modelling FG-TPMS plates. Practically, computational approaches based on higher-order shear deformation theories with five variables have been widely used because they can capture the nonlinear distribution of shear terms through the thickness of the plate and satisfy the zero-shear strains/stresses without taking into account shear correction factors (SCF). Numerous recent research on HSDT considers the justified distribution function [23]. It was seen that better results could be obtained as indicated in many reports including third-order shear deformation theory (TSDT) [25, 26], fifth-order shear deformation theory (FiSDT) [27], various trigonometric shear deformation theories [28, 29] and so on. However, the C^1 continuity in HSDT models causes difficulties in implementing itself into the standard finite elements. To address this issue, isogeometric analysis based on NURBS is adopted to fulfill naturally the high-order derivatives in the weak form.

Isogeometric analysis (IGA) coined by Hughes *et al.* [30] allows us to fill the gap between finite element analysis (FEA) and computer-aided design (CAD). IGA used the same NURBS-based basis functions to model the exact geometry and

approximate the FE solution. When IGA is used, accessing the CAD system during the FEA process is unnecessary and the exact geometry is unchanged at all discretization levels. IGA has been successfully applied to laminated composite plate/shell structures [31, 32, 24, 33, 34], functionally graded material (FGM) structure [35, 36, 37, 38]. Several advanced IGA techniques [39, 40, 41] have also been developed to enhance the approximation of the laminated composite structure.

In the current work, the mechanical behaviors of FG-TPMS plates are inspected according to the change in the relative density, or the porous characteristic of materials. A new fitting method is proposed based on a two-phase piece-wise function to fit and predict the effective features of FG-TPM plates. The higher-order shear deformation theories (HSDTs) are then employed to approximate the displacement field. After deriving the weak form, the NURBS-based isogeometric approach is then used to analyze static, buckling, and free vibration behaviors of FG-TPMS plates. In this study, three types of TPMS are adopted in the plate structures, whose properties depend on the relative density varying gradually through the plate thickness. Various plates with different porosity are utilized to describe the efficiency of these new porous plates.

2 Mechanical properties of FG-TPMS materials

In this section, A novel fitting approach is proposed to investigate the mechanical characteristics of the FG-TPMS foam structure. This study focuses on the FG-TPMS plate model based on three different types of sheet-based architecture including Primitive, Gyroid, and I-graph and wrapped package-graph (IWP). They can be described by Eqs. (1), and (3), which provide the sheet-based solid type constructed from TPMS geometry.

$$\begin{aligned}
\text{Primitive} \quad \phi &= \cos(w_1x_1) + \cos(w_2x_2) + \cos(w_3x_3), \\
\text{Gyroid} \quad \phi &= \sin(w_1x_1)\cos(w_2x_2) + \sin(w_2x_2)\cos(w_3x_3) + \sin(w_3x_3)\cos(w_1x_1), \\
\text{IWP} \quad \phi &= 2(\cos(w_1x_1)\cos(w_2x_2) + \cos(w_2x_2)\cos(w_3x_3) + \cos(w_3x_3)\cos(w_1x_1)) \\
&\quad - (\cos(2w_1x_1) + \cos(2w_2x_2) + \cos(2w_3x_3)).
\end{aligned} \tag{1}$$

where

$$w_i = \frac{2\pi n_i}{l_i}, i = 1, 2, 3 \tag{2}$$

where $\mathbf{x} = (x_1, x_2, x_3)^T$ denotes an arbitrary point in a three-dimensional domain, n_i and l_i indicate the unit cell quantity and its lengths, respectively. In this study, the same unit properties are applied to all three perpendicular directions.

$$-t \leq \phi \leq t \tag{3}$$

where t is the TPMS control parameter. The relationships of t and the relative density (ρ) of TPMS types are different from each other. Fig. 1 presents the fitting curves of the sheet-based TPMS relationship. In addition, ρ is defined by

$$\rho = \frac{V}{V_s} \tag{4}$$

in which V and V_s are the total volumes of the TPMS cell and the surrounding cube, respectively.

Fig. 2 demonstrates two groups of density distribution patterns through the plate thickness. These functions can be described in Eq. (5):

$$\rho = \begin{cases} \rho_{min} + (\rho_{max} - \rho_{min}) \times \left(\frac{x_3}{h} + \frac{1}{2} \right)^n, & \text{Pattern A} \\ \rho_{min} + (\rho_{max} - \rho_{min}) \times \left(1 - \cos\left(\frac{\pi x_3}{h} \right) \right)^n. & \text{Pattern B} \end{cases} \tag{5}$$

These distribution groups consist of non-uniform functions whose ranges vary from ρ_{min} to ρ_{max} . Using the power n , various relative density functions can be produced. In fact, numerical investigations on the influence of these parameters on the plate behaviors are implemented in Section 4. Fig. 3 illustrates three types of TPMS structures which are P, G, and IWP with density distribution pattern A and the power value of 3.

Regarding the elastic properties, the parent (base) material is assumed to be isotropic. In addition, the representative volume elements (RVE) of TPMS structures are indicated as cubic symmetric materials [42]. Their elasticity material

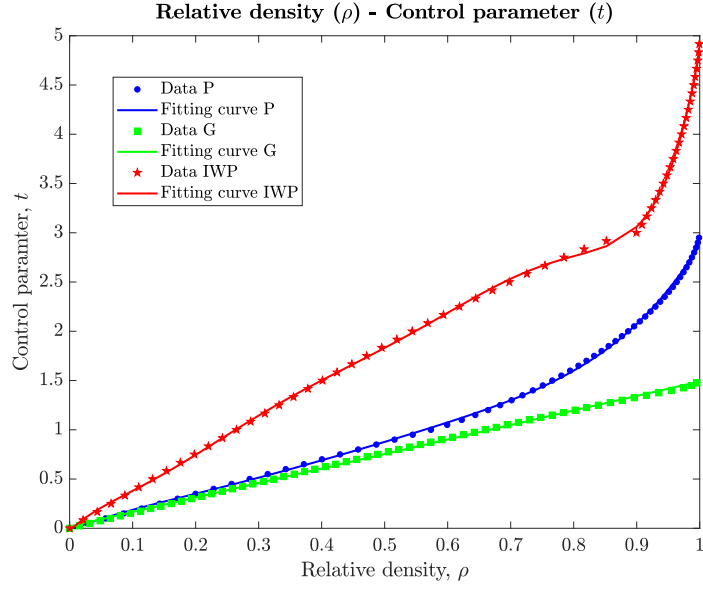
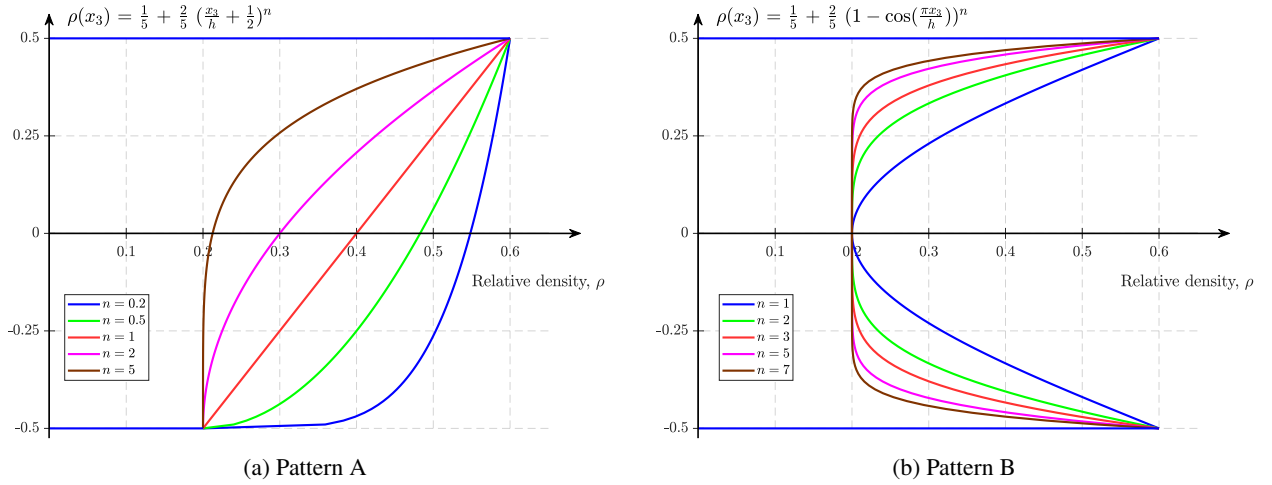
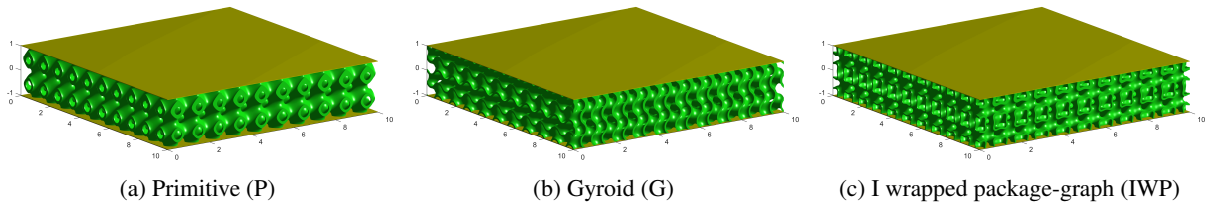
Figure 1: Relationship of control parameter t and relative density ρ of sheet-based TPMS

Figure 2: Relative density distribution of FG-TPMS

Figure 3: An illustration for FG-TPMS plate model with density pattern A and the power $n = 3$.

coefficients are expressed as an "isotropic-like form" as follows

$$\mathbf{C} = \begin{bmatrix} \lambda + 2\mu & \lambda & \lambda & 0 & 0 & 0 \\ & \lambda + 2\mu & \lambda & 0 & 0 & 0 \\ & & \lambda + 2\mu & 0 & 0 & 0 \\ & sym & & G & 0 & 0 \\ & & & & G & 0 \\ & & & & & G \end{bmatrix} \quad (6)$$

where $\lambda = \frac{E\nu}{(1+\nu)(1-2\nu)}$, and $\mu = \frac{E}{2(1+\nu)}$ describe the elastic Lamé coefficients, and a material is isotropic if $G = \mu$. In other words, G depends on the relative density ρ .

To apply the TPMS geometry in practice, all three independent variables including uniaxial elastic modulus (E), shear modulus (G), and Poisson's ratio (ν) of the TPMS cell need to be defined explicitly. Furthermore, Poisson's ratio is derived from the bulk modulus (K) using Eq. (7). These mechanical moduli of porous structures can be written in a scalar form based on the base material as described in Eq. (8).

$$\nu = \frac{3K - E}{6K} \quad (7)$$

$$E^* = \frac{E}{E_s}; \quad G^* = \frac{G}{G_s}; \quad K^* = \frac{K}{K_s}. \quad (8)$$

where E , G , and K are the elastic modulus, shear modulus, and bulk modulus of the TPMS cell, respectively; the corresponding properties of the parent (base) or isotropic elastic material are denoted as E_s , G_s , and K_s , respectively.

In recent studies, the effective mechanical properties of sheet-based TPMS structures were established using the power scaling law of cellular structure in the context of the relative density ρ [43]. However, the value of relative density might not be studied in the full range of 0 to 1, and the differences in mechanical responses of structures with various porous states were also ignored. In the current work, we propose a fitting method that can be divided into three continuous processes. At first, the elastic moduli of the structures are approximated by a two-phase piece-wise function based on their deformation modes. Next, the step values in the previous results are adopted to fit the shear and bulk moduli with the same function. Finally, the Poisson's ratios of these structures are generated by the relationship among the mechanical properties and estimated by another piece-wise function. This fitting process is shown in the flowchart in Fig. 4

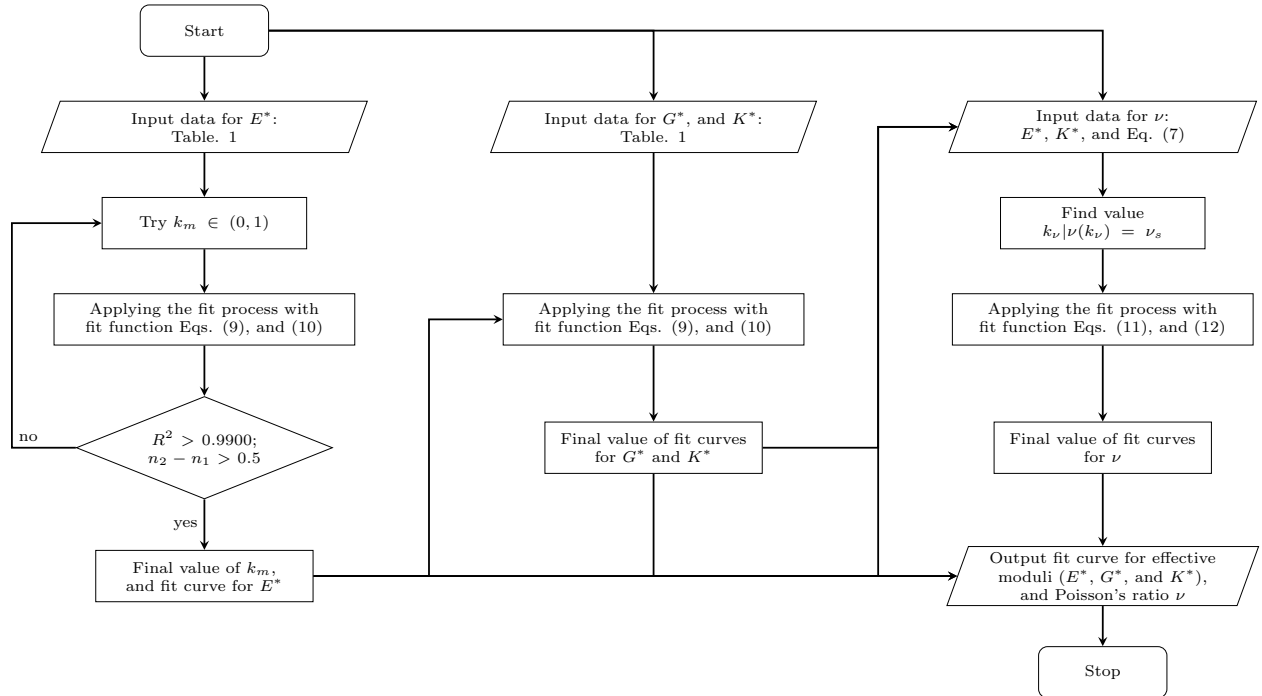


Figure 4: A flowchart for computing the effective mechanical properties using the fitting method.

The mechanical moduli of the TPMSs, namely elastic modulus, shear modulus, and bulk modulus are fitted by a two-phase model in Eq. (9). In this function, the coefficients can be minimized, bringing the value from 6 to 4, due to two conditions. They are the continuous condition at $\rho = k_m$ and the boundary condition at $\rho = 1$ which leads to $E^* = 1$. These conditions are described in Eq. (10):

$$E^* = \begin{cases} C_1 \rho^{n_1}, & \rho \leq k_m \\ C_2 \rho^{n_2} + C_3, & \rho > k_m \end{cases} \quad (9)$$

$$\begin{array}{ll} \text{Continuous Condition} & C_1 k_m^{n_1} = C_2 k_m^{n_2} + C_3 \\ \text{Boundary Condition} & C_2 + C_3 = 1. \end{array} \quad (10)$$

Consequently, the two coefficients, $C_2 = (C_1 k_m^{n_1} - 1)/(k_m^{n_2} - 1)$ and $C_3 = 1 - C_2$, can be calculated. In addition, the power coefficients (n_1 and n_2) depend on the behavior of the structure under the specific load type. These values are close to unity if the structure has a stretching-dominated mode, and are close to 2 if the structure has a bending-dominated mode. Moreover, this behavior mode depends not only on the geometry but also on the thickness of the walls in the sheet-based TPMS [44, 45]. Hence, the value k_m might be used to determine the separated region for each mode. However, this value might not coincide with all three moduli.

In this study, the value of k_m is selected first based on the strong difference in deformation modes of two relative density regions subjected to uniaxial load. This allows the power n_2 to reach a higher value than the value of n_1 because of the shifting from the stretching-dominated mode to the bending-dominated mode. The value of k_m is equal to 0.25, 0.45, and 0.35 for types P, G, and IWP, respectively. For instance, in the Primitive case, the second region is found to be fully bending while stretching mode can be observed for both regions of the IWP structure. While the Gyroid structure walls, however, might be stated to be always bending while carrying load despite any value of relative density. Therefore, the second region of this TPMS can be split due to the value of n_2 which is higher than 2. Furthermore, it is interesting to note that this k_m value can be further employed in simple shear and hydrostatic compression responses with high accuracy in fitting results.

As a result, the remaining coefficients are C_1 , n_1 , and n_2 . While the power coefficients (n_1 and n_2) provide the deformation modes, the coefficient C_1 indicates the material alignment to the loading direction. Moreover, this C_1 coefficient is also sensitive to fabrication imperfections, namely printing defects, solidification cracks or voids, relative density deviation, etc. Consequently, this coefficient might receive a smaller value in the experiment.

Although numerous studies on TPMS properties have been published, the mechanical behaviors of these structures have been shown to depend on the material scale and the number of units in the specimen. In fact, Simsek *et al.* [46] indicated that the 20% relative density sheet-based TPMS blocks with at least four layers could provide the constant elastic modulus which was consistent with micro-mechanics simulation results. This affirmation could be inappropriate with different relative densities; however, this feature is not within the scope of this study. Therefore, in adopted resources, the effective moduli were investigated for one representative unit cell using micro-mechanics simulations involving the periodic boundary condition. By employing the fitting tool, the effective properties equation can be generated with high accuracy. For the purpose of relative density investigation, the data used in the fitting process are collected from two of the previous key studies; one provides data in the range of 0 to 0.15, and the other covers the range of 0.15 to 0.8. In addition, these studies employed the same parent material properties i.e. isotropic solid with the elastic modulus (E_s) and Poisson's ratio ($\nu_s = 0.3$). The publications data that have been used in the fitting process are given in Table 1.

The final factors of the fitting curve for the effective elastic modulus, shear modulus, and bulk modulus are listed in Table 2. These fitting curves are compared with other data from several previous investigations which were not used in the fitting data, and these studies are included in Table 1. As shown in Fig. 5, the homogenization expression in the present study shows accurate predictions of the effective moduli of sheet-based TPMS structures.

For the uniaxial response, the power values of the first region (n_1) of all three structures are higher than unity, which means that both stretching and bending modes can be found during deformation. This corresponds to the new type of structure (shellular) [52]. The Primitive has the value of this coefficient being 1.264, and this result is close to the value of 1.17 reported in [44]. A similar result is also obtained with IWP ($n_1 = 1.225$). In contrast, Gyroid reaches the highest value ($n_1 = 1.467$), which shows that the bending mode appears to be significant even under low relative density. The comparable values of these power coefficients could also be found in [48, 50] and [49, 53] for IWP and Gyroid structures, respectively. Moreover, a large difference in the deformation behavior of these TPMSs is observed from the value of the second region power coefficient (n_2). For instance, as the relative density reaches 0.25, Primitive provides mostly bending mode with this value being approximately 2. In the case of IWP structure, stretching-dominated deformation can occur with any state of porosity ($n_2 = 1.782$). An exceptional value of this power coefficient belongs to the Gyroid structure. This value indicates the combination of bending and another deformation mode which results in a higher value of the power coefficient taking 2.351.

Furthermore, the region-splitting values (k_m) for elastic modulus show high accuracy on both shear modulus and bulk modulus. Specifically, in the light foam region which has been mainly investigated in previous studies, the shear response of P-type TPMS is suggested as a stretching-dominated deformation ($n_1 = 1.189$) which was reported by Lee *et al.* [44]. The power coefficient of 1.544 is slightly greater than the value of 1.33 achieved in [2]. However, both values indicate the combination of stretching and bending behaviors of the Gyroid structure. A similar agreement can be concluded with IWP according to the publication of Abu Al-Rub *et al.* [50]. In the case of hydrostatic load, the

Table 1: Published data used in the present study

Property	TPMS	Adopted sources		Comparison sources
		Light foam	Heavy foam	
Elastic modulus, E	Primitive	[2]	[45]	[44, 47, 48, 10, 20]
	Gyroid	[2]	[45]	[3, 47, 49, 10, 20]
	IWP	[2]	[45]	[50, 48, 51, 10, 20]
Shear modulus, G	Primitive	[2]	[45]	[44, 47]
	Gyroid	[2]	[45]	[3, 47]
	IWP	[2]	[45]	[50]
Bulk modulus, K	Primitive	[2]	[47]	[44]
	Gyroid	[3]	[47]	[2]
	IWP	[2]	[2]	[50]

bulk modulus power coefficients (n_1) of 1.127, 1.240, and 1.064 are equivalent to the values of 0.980, 1.649, and 1.072 corresponding to P, G, and IWP structures listed in the comparison sources. However, due to the lack of data on the heavy foam region of IWP bulk modulus, we only provide the fitting results of the first region of this TPMS. In other words, these values might be varied when different splitting points k_m of each structure are chosen.

The Poisson's ratio (ν) of the aforementioned TPMSs can be generated along with the fitting results of uniaxial and hydrostatic modulus given by Eq. (7). However, a similar fitting approach to other mechanical properties might simplify the above expression for application. A piece-wise formulation with an exponential function at the first region and a quadratic function at the other one as in Eq. (11) is investigated in this study. The major difference between the two proposed functions is that the two regions of the second formulation are separated by a value of relative density (k_v) which provides Poisson's ratio of the parent material (i.e. $\nu = \nu_s$). This assumption was concluded from the similar tendencies of considering TPMSs and could be considered a two-phase continuous condition. In addition, at fully dense material, the Poisson's ratio value needs to be consistent with the constituent material. The mathematical equations for these conditions are shown in Eq. (12):

$$\nu = \begin{cases} a_1 e^{b_1 \rho} + d_1, & \rho \leq k_v \\ a_2 \rho^2 + b_2 \rho + d_2, & \rho > k_v \end{cases} \quad (11)$$

$$\begin{aligned} 1^{st} \text{ Continuous Condition} & \quad a_1 e^{b_1 k_v} + d_1 = \nu_s \\ 2^{nd} \text{ Continuous Condition} & \quad a_2 k_v^2 + b_2 k_v + d_2 = \nu_s \\ \text{Boundary Condition} & \quad a_2 + b_2 + d_2 = \nu_s. \end{aligned} \quad (12)$$

In fact, the coefficient k_v can be pre-defined according to the constituent material Poisson's ratio in this study ($\nu_s = 0.3$). This coefficient value can be considered the common value in metallic materials. Generally, three independent coefficients (a_1 , a_2 , and b_1) are chosen to create the homogenization function. The others could be generated by using the above boundary conditions as $d_1 = \nu_s - a_1 e^{b_1 k_v}$, $b_2 = -a_2(k_v + 1)$, and $d_2 = \nu_s - a_2 - b_2$. Poisson's ratio curve coefficients and graphs after the fitting process are shown in Table 3 and Fig. 6, respectively. The IWP structure could be fitted using this strategy despite the missing data, and Poisson's ratio value of this structure in the heavy foam region might be considered a prediction. Nonetheless, it is suggested that these fitting results should only be applied while Poisson's ratio of the constituent material coincides with the fitting data. TPMS structures fabricated by various parent materials might behave differently in this property due to the divergence in effective bulk modulus (K^*). In general, this fitting strategy can give a good estimation of the subordination of Poisson's ratio on the relative density of TPMS structures.

Table 2: Fitting curves for the effective elastic modulus, shear modulus, and bulk modulus

Effective property	TPMS	C_1	n_1	n_2	Expression	R -square	Adjusted R -square
Elastic modulus, E^*	Primitive	0.317	1.264	2.006	$E^* = \begin{cases} 0.317\rho^{1.264}, & \rho \leq 0.25 \\ 1.007\rho^{2.006} - 0.007, & \rho > 0.25 \end{cases}$	0.9998	0.9998
	Gyroid	0.596	1.467	2.351	$E^* = \begin{cases} 0.596\rho^{1.467}, & \rho \leq 0.45 \\ 0.962\rho^{2.351} + 0.038, & \rho > 0.45 \end{cases}$	0.9996	0.9995
	IWP	0.597	1.225	1.782	$E^* = \begin{cases} 0.597\rho^{1.225}, & \rho \leq 0.35 \\ 0.987\rho^{1.782} + 0.013, & \rho > 0.35 \end{cases}$	0.9968	0.9959
Shear modulus, G^*	Primitive	0.705	1.189	1.715	$G^* = \begin{cases} 0.705\rho^{1.189}, & \rho \leq 0.25 \\ 0.953\rho^{1.715} + 0.047, & \rho > 0.25 \end{cases}$	0.9996	0.9996
	Gyroid	0.777	1.544	1.982	$G^* = \begin{cases} 0.777\rho^{1.544}, & \rho \leq 0.45 \\ 0.973\rho^{1.982} + 0.027, & \rho > 0.45 \end{cases}$	0.9999	0.9998
	IWP	0.529	1.287	2.188	$G^* = \begin{cases} 0.529\rho^{1.287}, & \rho \leq 0.35 \\ 0.960\rho^{2.188} + 0.040, & \rho > 0.35 \end{cases}$	0.9999	0.9999
Bulk modulus, K^*	Primitive	0.487	1.127	2.380	$K^* = \begin{cases} 0.487\rho^{1.127}, & \rho \leq 0.25 \\ 0.932\rho^{2.380} + 0.068, & \rho > 0.25 \end{cases}$	0.9993	0.9992
	Gyroid	0.536	1.240	3.336	$K^* = \begin{cases} 0.536\rho^{1.240}, & \rho \leq 0.45 \\ 0.861\rho^{3.336} + 0.139, & \rho > 0.45 \end{cases}$	0.9988	0.9986
	IWP	0.439	1.064		$K^* = 0.439\rho^{1.064}, \rho \leq 0.35$	0.9990	0.9987

Table 3: Fitting curve for Poisson's ratio

TPMS	a_1	b_1	a_2	Expression	R -square	Adjusted R -square
Primitive	0.314	-1.004	0.152	$\nu = \begin{cases} 0.314e^{-1.004\rho} + 0.119, & \rho \leq 0.55 \\ 0.152\rho^2 - 0.235\rho + 0.383, & \rho > 0.55 \end{cases}$	0.9862	0.9856
Gyroid	0.192	-1.349	0.402	$\nu = \begin{cases} 0.192e^{-1.349\rho} + 0.202, & \rho \leq 0.50 \\ 0.402\rho^2 - 0.603\rho + 0.501, & \rho > 0.50 \end{cases}$	0.9879	0.9874
IWP	2.597	-0.157	0.201	$\nu = \begin{cases} 2.597e^{-0.157\rho} - 2.244, & \rho \leq 0.13 \\ 0.201\rho^2 - 0.227\rho + 0.326, & \rho > 0.13 \end{cases}$	0.9932	0.9923

3 Isogeometric analysis of FG-TPMS plates

3.1 Configuration of FG-TPMS plates

In the current study, the FG-TPMS plate is described as a porous plate with an FG-TPMS core and two skin layers at both top and bottom of the plate. As presented in the previous section, the gradation approach is utilized for the TPMS

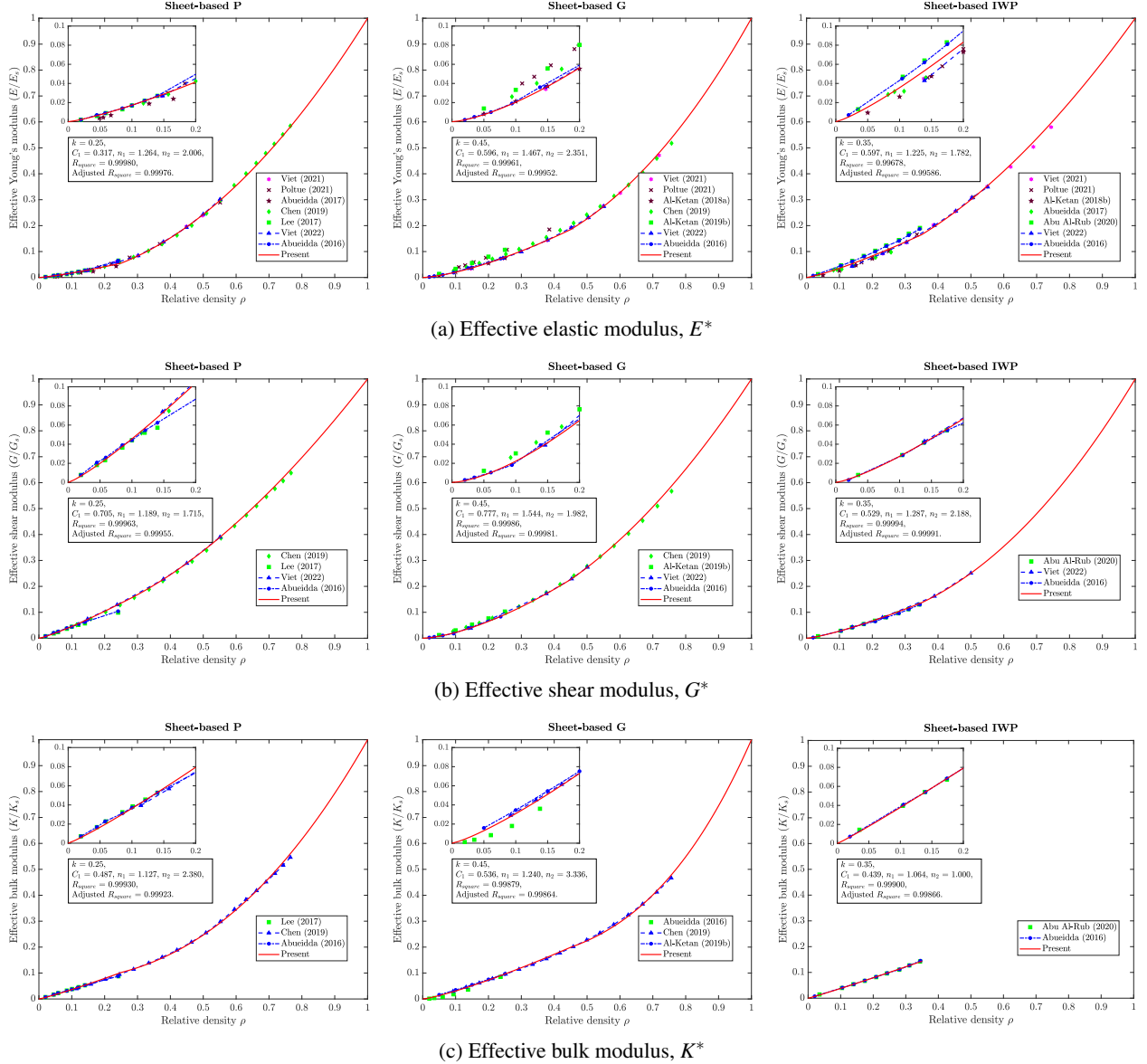


Figure 5: Effective mechanical moduli of Primitive, Gyroid, and IWP.

shell thickness by changing the control parameter t of the implicit function. We propose two main functional patterns for gradation that are given in Eq. (5). The Cartesian coordinate system in physics is set as in Fig. 7, where the plate mid-plane is adopted as the x_1Ox_2 plane and the x_3 direction demonstrates the plate thickness. The symbols a , b , and h denote the dimension of the plate in the x_1 , x_2 , and x_3 axes, respectively. In addition, the thickness-to-length ratio ranging from 0.005 to 0.2 is applied in the numerical example to provide various views of both thin and thick plate behaviors. Furthermore, the skin layers of this plate might be fabricated simultaneously or separately from the inner core, using the same material. It is suggested that these skins are only used as a uniform load transmission and should not be included in the analysis. To reduce their influences on the comprehensive performance of the FG-TPMS plate, the maximum value of their thickness is set to be smaller than $0.001h$. With this minor value, the contributions of these layers to all the in-plane, flexural, and shear stiffness can be negligible (e.g. less than 1%).

To yield accurate solutions, a five-variable SeSD plate model, which is coincided for both thick and thin plates, is utilized. The assumptions for this model can be listed as follows

- Both bending stress and shell stress are taken into account, therefore, the displacement of all three directions are considered variables.

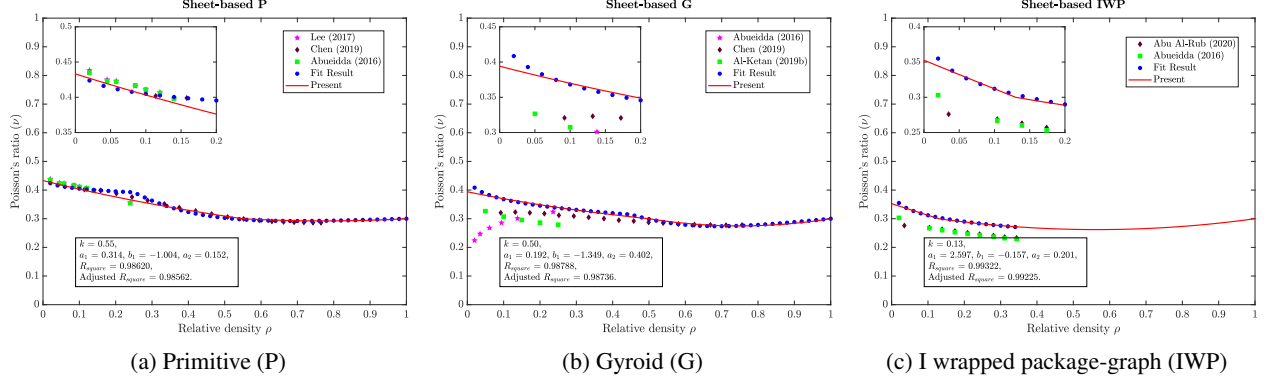
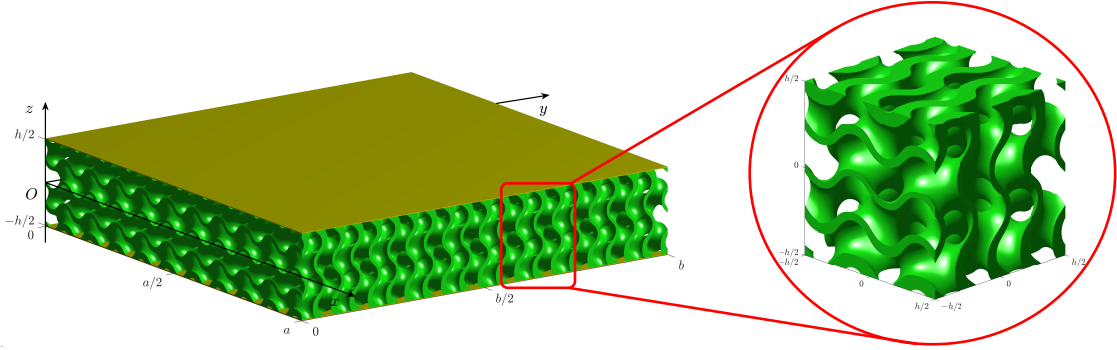


Figure 6: Poisson's ratio of Primitive, Gyroid, and IWP.

Figure 7: A detailed zoom of FGP-TPMS type G with density pattern B and the power $n = 1$.

- As the impact of shear deformation on the flexural responses of the plate, the angles of a plate's line in x_3 direction after deformation with both in-plane axis are denoted as rotations variables.
- The shear stress and strain along the plate thickness can be expressed in a nonlinear function.
- The out-of-plane normal stress is negligible compared to others. This stress equals zero in the calculation. The bending stiffness of FG-TPMS could be generated by this presumption from the constitutive matrix in Eq. (6).

The mathematical description of the FG-TPMS plate can be provided with the following descriptions. Let us consider a domain Ω bounded in \mathbb{R}^2 as a mid-plane surface of an FG-TPMS plate, cf. Fig. 3. Let $\mathbf{u}_0 = (u_{10}, u_{20}, u_{30})^T$ be the in-plane displacements and the transverse displacement, while $\beta = (\beta_1, \beta_2)^T$ are the rotations about the x_1 and x_2 axes. The plate made of FG-TPMS with elastic modulus E , shear modulus G , and Poisson's ratio ν is defined. A displacement field according to HSDT is widely used as

$$\begin{aligned} u_1(x_1, x_2, x_3) &= u_{10}(x_1, x_2) - x_3 u_{3,1} + f(x_3) \beta_1(x_1, x_2) \\ u_2(x_1, x_2, x_3) &= u_{20}(x_1, x_2) - x_3 u_{3,2} + f(x_3) \beta_2(x_1, x_2) \\ u_3(x_1, x_2, x_3) &= u_{30}(x_1, x_2) \end{aligned} \quad (13)$$

where $f(x_3)$ is a shear strain shape function controlling the nonlinear distribution of shear stresses and strains through the plate thickness. According to the previous work [23], the shape functions available can be unified by polynomial forms. Therefore, a seventh-order shear deformation theory (SeSDT) is used for the present study to model and compute the FG-TPMS plate. A different form of above equations can be written as

$$\mathbf{u} = \mathbf{u}_0 + x_3 \mathbf{u}_1 + f(x_3) \mathbf{u}_2 \quad (14)$$

in which

$$\mathbf{u}_1 = \{-u_{3,1}, -u_{3,2}, 0\}^T, \mathbf{u}_2 = \{\beta_1, \beta_2, 0\}^T \quad (15)$$

3.2 Discrete governing equations

From the definitions of the plate displacement field, the in-plane and transverse shear strains become

$$\boldsymbol{\varepsilon} = \boldsymbol{\varepsilon}_0 + x_3 \boldsymbol{\varepsilon}_1 + f(x_3) \boldsymbol{\varepsilon}_2 = [1 \quad x_3 \quad f(x_3)] \boldsymbol{\varepsilon}_p, \quad \gamma = f'(x_3) \boldsymbol{\varepsilon}_s \quad (16)$$

where

$$\begin{aligned} \boldsymbol{\varepsilon}_p &= \begin{bmatrix} \boldsymbol{\varepsilon}_0 \\ \boldsymbol{\varepsilon}_1 \\ \boldsymbol{\varepsilon}_2 \end{bmatrix}; \boldsymbol{\varepsilon}_0 = \begin{bmatrix} u_{10,1} \\ u_{20,2} \\ u_{10,2} + u_{20,1} \end{bmatrix} \\ \boldsymbol{\varepsilon}_1 &= - \begin{bmatrix} u_{3,11} \\ u_{3,22} \\ 2u_{3,12} \end{bmatrix}; \boldsymbol{\varepsilon}_2 = \begin{bmatrix} \beta_{1,1} \\ \beta_{2,2} \\ \beta_{1,2} + \beta_{2,1} \end{bmatrix}; \boldsymbol{\varepsilon}_s = \begin{bmatrix} \beta_1 \\ \beta_2 \end{bmatrix} \end{aligned} \quad (17)$$

Next we define the following material matrices

$$\mathbf{D}_p = \begin{bmatrix} \mathbf{A} & \mathbf{B} & \mathbf{E} \\ \mathbf{B} & \mathbf{D} & \mathbf{F} \\ \mathbf{E} & \mathbf{F} & \mathbf{H} \end{bmatrix} \quad (18)$$

where

$$\begin{aligned} [A_{ij}, B_{ij}, D_{ij}, E_{ij}, F_{ij}, H_{ij}] &= \int_{-\frac{h}{2}}^{\frac{h}{2}} [1, x_3, x_3^2, f(x_3), x_3 f(x_3), f(x_3)^2] \bar{C}_{ij} dx_3 \\ D_{ij}^s &= \int_{-\frac{h}{2}}^{\frac{h}{2}} f'(x_3)^2 G_{ij} dx_3 \end{aligned} \quad (19)$$

and h is the plate thickness and \bar{C}_{ij}, G_{ij} are the tensors derived from

$$\bar{\mathbf{C}} = \begin{bmatrix} \frac{E}{1-\nu^2} & \frac{E\nu}{1-\nu^2} & 0 \\ \frac{E\nu}{1-\nu^2} & \frac{E}{1-\nu^2} & 0 \\ 0 & 0 & G \end{bmatrix}; \bar{\mathbf{G}} = G \begin{bmatrix} 1 & 0 \\ 0 & 1 \end{bmatrix} \quad (20)$$

Let \mathcal{V} and \mathcal{V}_0 be denoted as

$$\mathcal{V} = \{ \tilde{\mathbf{u}} = (\mathbf{u}_0, \boldsymbol{\beta}) : \mathbf{u}_0 \in H^1(\Omega)^2 \times H^2(\Omega), \boldsymbol{\beta} \in H^1(\Omega)^2 \} \cap \mathcal{B} \quad (21)$$

$$\mathcal{V}_0 = \{ \tilde{\mathbf{v}} = (\mathbf{v}_0, \boldsymbol{\eta}) : \mathbf{v}_0 \in H^1(\Omega)^2 \times H^2(\Omega), \boldsymbol{\eta} \in H^1(\Omega)^2 : \mathbf{v}_0 = \mathbf{0}, \boldsymbol{\eta} = \mathbf{0} \text{ on } \partial\Omega \} \quad (22)$$

with \mathcal{B} being a set of the essential boundary conditions.

A weak form of the static analysis is to seek $\tilde{\mathbf{u}} \in \mathcal{V}$ such that

$$\forall \tilde{\mathbf{v}} \in \mathcal{V}_0, \quad a_p(\tilde{\mathbf{v}}, \tilde{\mathbf{u}}) + a_s(\boldsymbol{\eta}, \boldsymbol{\beta}) = (\tilde{v}_3, q) \quad (23)$$

where q is a transverse load; meanwhile the scalar and bilinear operators are expressed by

$$a_p(\tilde{\mathbf{v}}, \tilde{\mathbf{u}}) = \int_{\Omega} \boldsymbol{\varepsilon}_p(\tilde{\mathbf{v}}) : \mathbf{D}_p : \boldsymbol{\varepsilon}_p(\tilde{\mathbf{u}}) d\Omega, \quad a_s(\boldsymbol{\eta}, \boldsymbol{\beta}) = \int_{\Omega} \boldsymbol{\varepsilon}_s(\boldsymbol{\eta}) : \mathbf{D}^s : \boldsymbol{\varepsilon}_s(\boldsymbol{\beta}) d\Omega, \quad (v_3, u_3) = \int_{\Omega} v_3 u_3 d\Omega \quad (24)$$

In the case of free vibration analysis, a weak form is to find $\omega \in \mathbb{R}^+$ and $\mathbf{0} \neq \tilde{\mathbf{u}} \in \mathcal{V}$ such that

$$\forall \tilde{\mathbf{v}} \in \mathcal{V}_0, \quad a_p(\tilde{\mathbf{v}}, \tilde{\mathbf{u}}) + a_s(\boldsymbol{\eta}, \boldsymbol{\beta}) = \omega^2 a_m(\tilde{\mathbf{v}}, \tilde{\mathbf{u}}) \quad (25)$$

where

$$a_m(\tilde{\mathbf{v}}, \tilde{\mathbf{u}}) = \int_{\Omega} \begin{bmatrix} \mathbf{v}_0 \\ \mathbf{v}_1 \\ \mathbf{v}_2 \end{bmatrix}^T \tilde{\mathbf{m}} \begin{bmatrix} \mathbf{u}_0 \\ \mathbf{u}_1 \\ \mathbf{u}_2 \end{bmatrix} d\Omega, \quad (26)$$

$$\tilde{m}_{ij} = \tilde{m}_{ji}, \quad [(\tilde{m}_{11}, \tilde{m}_{12}, \tilde{m}_{13}, \tilde{m}_{22}, \tilde{m}_{23}, \tilde{m}_{33})] = \int_{-\frac{h}{2}}^{\frac{h}{2}} \rho(x_3) [1, x_3, x_3^2, f(x_3), x_3 f(x_3), f^2(x_3)] dx_3 \quad (27)$$

and ρ and ω denote the mass density and natural frequency, respectively.

For in-plane buckling behavior with pre-buckling stresses $\hat{\Sigma}_0$, the weak form associated with the gradients of transverse deflection is to seek $\lambda_{cr} \in \mathbb{R}^+$ and $\mathbf{0} \neq \tilde{\mathbf{u}} \in \mathcal{V}$ s.t.

$$\forall \tilde{\mathbf{v}} \in \mathcal{V}_0, \quad a_p(\tilde{\mathbf{v}}, \tilde{\mathbf{u}}) + a_s(\boldsymbol{\eta}, \boldsymbol{\beta}) = \lambda_{cr} \{ h a_g(\tilde{v}_3, u_3) \} \quad (28)$$

where

$$a_g(v_3, u_3) = \int_{\Omega} \nabla^T v_3 \hat{\Sigma}_0 \nabla u_3 d\Omega, \quad \hat{\Sigma}_0 = \begin{bmatrix} \boldsymbol{\sigma}_1^0 & \boldsymbol{\sigma}_{12}^0 \\ \boldsymbol{\sigma}_{12}^0 & \boldsymbol{\sigma}_2^0 \end{bmatrix} \quad (29)$$

where $\nabla = [\partial/\partial x_1 \quad \partial/\partial x_2]^T$ indicates the gradient operator, $\sigma_1^0 = \sigma_{cr}$, $\sigma_2^0 = \sigma_{12}^0 = 0$ and $\sigma_1^0 = \sigma_2^0 = \sigma_{cr}$, $\sigma_{12}^0 = 0$ stand for a uni-axial buckling analysis, and a bi-axial buckling analysis, respectively, where σ_{cr} denotes critical buckling load.

It can be seen from the bilinear term $a_p(\cdot, \cdot)$ that the second derivatives in the displacement variable, u_3 . Hence, approximate solutions require at least the C^1 continuity which causes difficulties using standard finite element methods. Alternatively, isogeometric analysis allows us to produce both exact geometry and arbitrarily high-order continuity. The next section describes numerical solutions using the NRUBS-based IGA.

3.3 NURBS-based IGA approximations

For the goal of this study, we mention only the basic background of isogeometric analysis. More details of the advanced techniques on IGA are provided in the textbook [54]. A knot vector $\Xi = \{\xi_1, \xi_2, \xi_3, \dots, \xi_{n+p+1}\}$, which increases in the interval of ξ_1 and ξ_{n+p+1} , is a primary component constituting NURBS basis functions. The B-spline basis functions provide non-negative values, C^{p-1} continuous at a single knot, and C^∞ continuous inside a knot span. A multiple knot means the same knot value repeated k times for the continuity up to C^{p-k} . To ease in numerical computations, an open knot vector which has the first and last knots repeated $(p+1)$ times, is used.

By using Cox-de Boor algorithm, B-spline basis functions $N_{i,p}(\xi)$ of order $p \geq 0$ in the one-dimensional (1D) space are compute by

$$N_{i,0}(\xi) = \begin{cases} 1 & \text{if } \xi_i \leq \xi < \xi_{i+1} \\ 0 & \text{otherwise} \end{cases} \quad (30)$$

$$N_{i,p}(\xi) = \frac{\xi - \xi_i}{\xi_{i+p} - \xi_i} N_{i,p-1}(\xi) + \frac{\xi_{i+p+1} - \xi}{\xi_{i+p+1} - \xi_{i+1}} N_{i+1,p-1}(\xi) \quad (31)$$

Two-dimensional (2D) NURBS basis functions are then denoted as follows

$$R_I(\xi, \chi) = \frac{N_{i,p}(\xi) M_{j,q}(\chi) w_{i,j}}{\sum_{i=1}^n \sum_{j=1}^m N_{i,p}(\xi) M_{j,q}(\chi) w_{i,j}} \quad (32)$$

where $N_{i,p}(\xi)$ and $M_{j,q}(\chi)$ are B-spline basis functions associated with two knot vectors Ξ and \mathbf{X} , respectively, and $w_{i,j}$ are the positive weights of i, j control points.

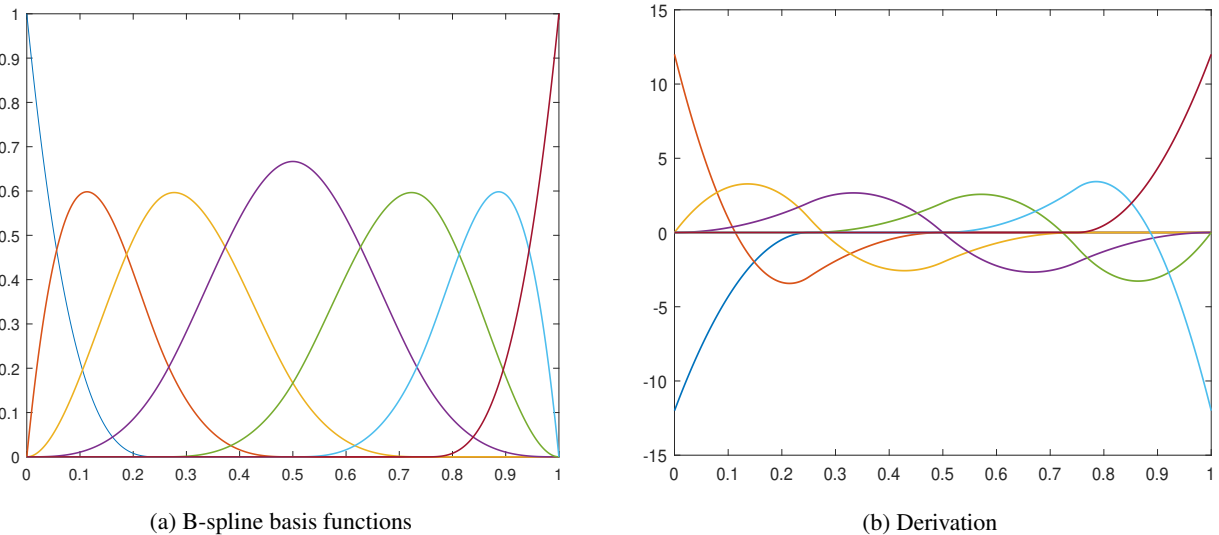


Figure 8: 1D 3rd-order B-spline basis functions and its derivation, $\Xi = \{0, 0, 0, 0, 1/4, 1/2, 3/4, 1, 1, 1, 1\}$.

Then the approximate solution $\tilde{\mathbf{u}}^h$ can be expressed using NURBS basis functions as follows

$$\tilde{\mathbf{u}}^h(\xi, \chi) = \sum_I^{m \times n} R_I(\xi, \chi) \mathbb{I}_{5 \times 5} \mathbf{d}_I \quad (33)$$

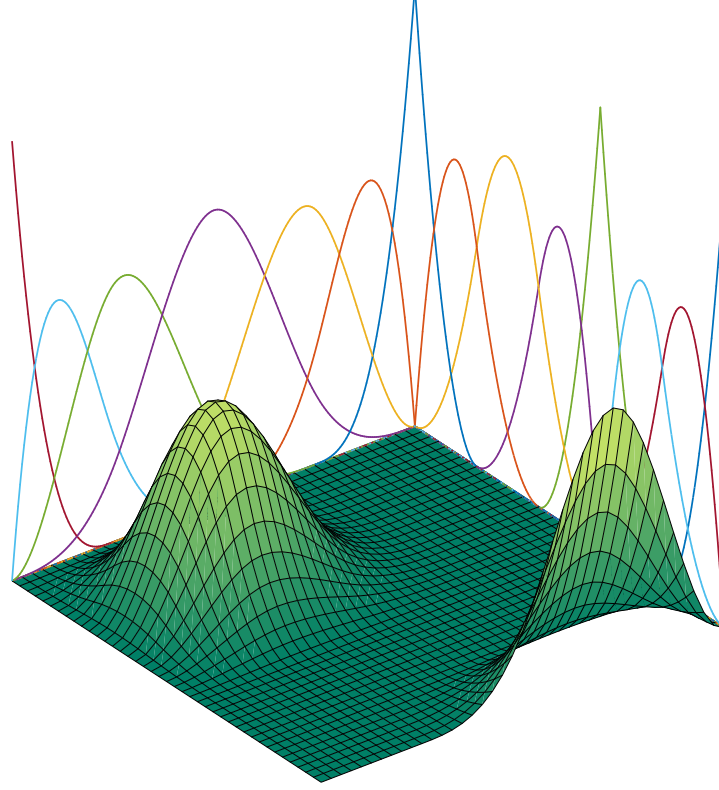


Figure 9: 2D B-spline basis functions associated with two knot vectors $\Xi = \{0, 0, 0, 0, 1/4, 1/2, 3/4, 1, 1, 1, 1\}$ and $\mathbf{X} = \{0, 0, 0, 1/5, 2/5, 3/5, 3/5, 1, 1, 1\}$.

For computations, the bounded domain Ω is divided into N_e patches such that $\Omega \approx \bigcup_{e=1}^{N_e} \Omega^e$ and $\Omega^i \cap \Omega^j = \emptyset$, $i \neq j$. The approximate solution of the static problem using NURBS basis functions for the FG-TPMS plate is to seek $\tilde{\mathbf{u}}^h \in \mathcal{V}^h$ such that

$$\forall \tilde{\mathbf{v}}^h \in \mathcal{V}_0^h, \quad a_p(\tilde{\mathbf{v}}^h, \tilde{\mathbf{u}}^h) + a_s(\boldsymbol{\eta}^h, \boldsymbol{\beta}^h) = (\tilde{v}_3^h, p) \quad (34)$$

where the NURBS patch spaces, \mathcal{V}^h and \mathcal{V}_0^h , are specified by

$$\mathcal{V}^h = \{\tilde{\mathbf{u}}^h = (\mathbf{u}_0^h, \boldsymbol{\beta}^h) \in \mathcal{V}, \mathbf{u}_0^h|_{\Omega^e} \in P_k(\Omega^e)^3, \boldsymbol{\beta}^h|_{\Omega^e} \in P_k(\Omega^e)^2\} \cap \mathcal{B} \quad (35)$$

$$\mathcal{V}_0^h = \{\tilde{\mathbf{v}}^h \in \mathcal{V}_0 : \tilde{\mathbf{v}}^h = \mathbf{0} \text{ on } \partial\Omega\} \quad (36)$$

where $P_k(\Omega^e)$ describes the set of NURBS bases of degree k for each approximate variable.

The NURBS-based solution for the free vibration problem is to determine the natural frequency $\omega^h \in \mathbb{R}^+$ and $\mathbf{0} \neq \tilde{\mathbf{u}}^h \in \mathcal{V}^h$ such that

$$\forall \tilde{\mathbf{v}}^h \in \mathcal{V}_0^h, \quad a_p(\tilde{\mathbf{v}}^h, \tilde{\mathbf{u}}^h) + a_s(\boldsymbol{\eta}^h, \boldsymbol{\beta}^h) = (\omega^h)^2 a_m(\tilde{\mathbf{v}}^h, \tilde{\mathbf{u}}^h) \quad (37)$$

Thus, isogeometric analysis is also used to find the critical buckling load (λ_{cr}^h) of the buckling problem where $\lambda_{cr}^h \in \mathbb{R}^+$ and $\mathbf{0} \neq \tilde{\mathbf{u}}^h \in \mathcal{V}^h$

$$\forall \tilde{\mathbf{v}}^h \in \mathcal{V}_0^h, \quad a_p(\tilde{\mathbf{v}}^h, \tilde{\mathbf{u}}^h) + a_s(\boldsymbol{\eta}^h, \boldsymbol{\beta}^h) = \lambda_{cr}^h \{h a_g(\tilde{v}_3^h, u_3^h)\} \quad (38)$$

It is worth emphasizing that in solving the aforementioned problems, several well-known numerical methods [54] are suitable candidates yet isogeometric analysis (IGA) is the most common choice to capture naturally high continuity in the weak form and achieve ultra-accuracy in solutions without any additional variables and computationally expensive requirements.

4 Numerical examples

In this section, the rectangular and circular plates with different architectures and boundary conditions are employed to validate the above IGA approach. Fig. 10 a) and b) demonstrate the simply supported (SSSS) and fully clamped (CCCC) boundary of rectangular plates. While the corresponding samples of circular plates are plotted in Fig. 11. To compare with previous studies, free vibration and buckling behaviors of isotropic plates are investigated. For the buckling analysis, rectangular plates subjected to uniaxial and biaxial compression are shown in Fig. 10 c) and d), respectively. Furthermore, to achieve good convergence results, the fine mesh with eleven refinements has been adopted for both rectangular and circular plates where an example of one refinement mesh is described in Fig. 12. As mentioned, the base materials adopted in this study are metallic materials that have the same Poisson's ratio of 0.3. Furthermore, a plastic material is also listed, whose Poisson's ratio is 0.33 instead, to emphasize the differences in this property. This dissimilarity between metallic and plastic TPMS structures is aimed at future investigations. The mechanical properties of these materials are tabulated in Table 4.

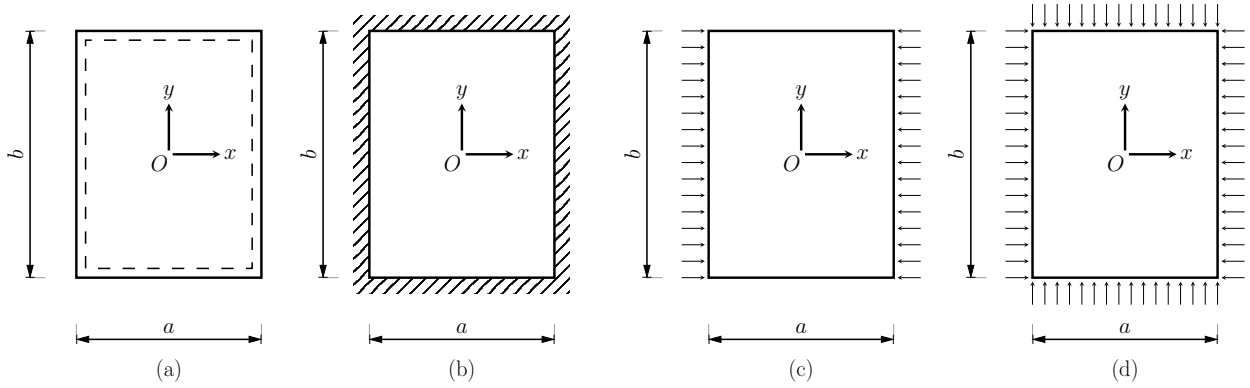


Figure 10: Rectangular plate: a) Simply supported plate, b) Fully clamped plate, c) Uniaxial compression along the x direction, d) Biaxial compression.

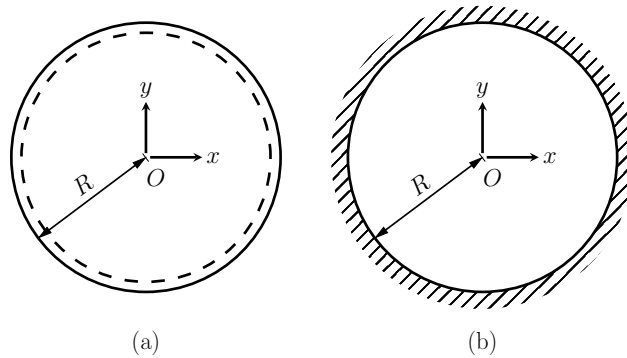


Figure 11: Circle plate: a) Simply supported plate, b) Fully clamped plate.

Table 4: Properties of parent materials

Material	E_s (GPa)	ρ_s (kg/m ³)	ν_s
Aluminum (Al)	70	2702	0.3
Steel (SUS304)	200	8000	0.3
Titanium (Ti)	106	4510	0.3
Copper	117	8960	0.3
Brass	90	8730	0.3
Polylactic acid (PLA)	3.15	1240	0.33

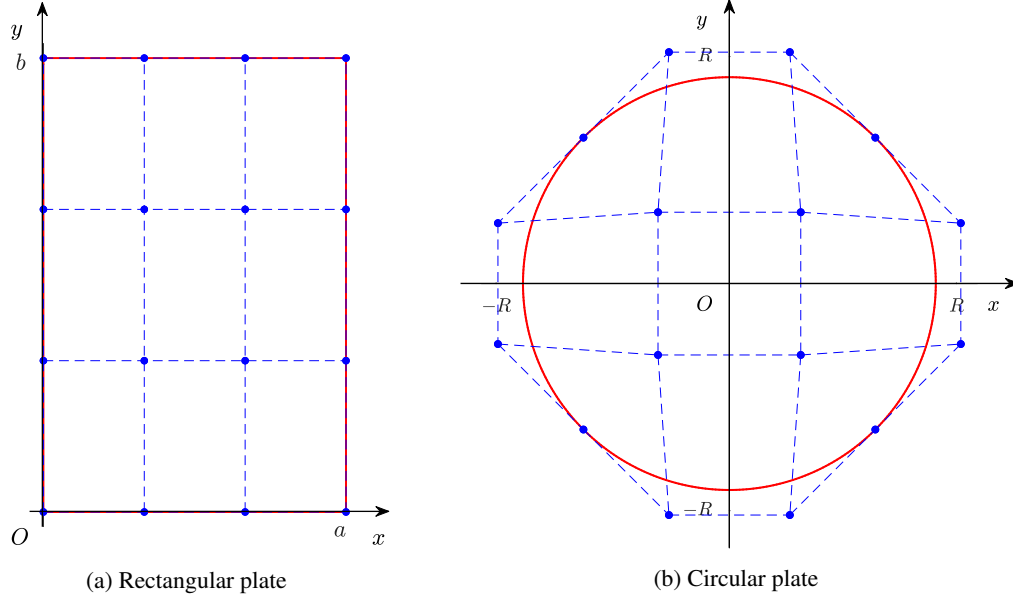


Figure 12: A coarse mesh with one NURBS element of rectangular and circular plates.

Next, six density distribution cases are utilized to illustrate the FG-TPMS plate behaviors. Their average relative densities are approximately 0.35. Therefore, they might be considered to be foam materials. This value of mean density was adopted in previous studies with functionally graded beams [20]. The corresponding coefficients of porosity distribution patterns A and B are provided in Table 5. Nevertheless, it is seen that various other scenarios of relative density distribution can be achieved from the changes in these coefficients.

Table 5: Six density distribution cases with the same average value of 0.35

Pattern	Case	ρ_{min}	ρ_{max}	n
A	A1	0.20	0.5	1.0
	A2	0.20	0.8	3.0
	A3	0.25	1.0	6.5
B	B1	0.20	0.5	0.561
	B2	0.20	0.8	1.757
	B3	0.25	1.0	3.943

Furthermore, Hashin-Shtrikman (HS) hypothesis can provide effective bulk and shear modulus boundaries for multiphase materials in terms of relative density [55]. By assigning one of the materials with zero stiffness, the HS upper boundary for porous structure could be introduced which is defined in Eqs. (39). Due to the isotropic characteristic assumption for both base and result materials, the uniaxial elastic modulus and Poisson's ratio of these porous structures can be described by Eqs. (40). A functionally graded porous plate (FGPP) with HS upper boundary mechanical properties is adopted to inspect the efficiency of TPMS geometries in functionally graded plate structures.

$$G_{HS} = G_s + \frac{1 - \rho}{\frac{1}{-G_s} + \frac{6(K_s + 2G_s)\rho}{5G_s(3K_s + 4G_s)}}; \quad K_{HS} = K_s + \frac{1 - \rho}{\frac{1}{-K_s} + \frac{3\rho}{3K_s + 4G_s}} \quad (39)$$

$$E_{HS} = \frac{9G_{HS}K_{HS}}{3K_{HS} + G_{HS}}; \quad \nu_{HS} = \frac{3K_{HS} - 2G_{HS}}{2(3K_{HS} + G_{HS})} \quad (40)$$

4.1 Static and buckling analysis

At first, the central deflection under a uniform distribution load of both isotropic and porous plates is computed using the new isogeometric approach in this study. The results are given in Table. 6 where solutions from other numerical

methods are adopted for comparisons, including finite element method FEM [56], and cell-based smoothed finite element method (CS-FEM) [57]. It can be seen that there is a remarkable agreement between the IGA approach and other methods with less than 1% in deviations. This highest value belongs to the case of the fully clamped plate with a high thickness-to-length ratio ($h/a = 0.1$). Next, the buckling analysis of these plates with different aspect ratios is observed by the above isogeometric approach in Table. 7. In addition to the analytical solutions by [58], an edge-based smoothed finite element method (ES-FEM) [59] has been adopted for verification. Consequently, the strong agreement between the isotropic results and these solutions can validate this method's efficacy.

Table 6: The normalized deflection of the center-point ($\bar{w}_c = w_c qa^4 / (100D)$) for square FG plates subjected to uniform load with various density distribution cases ($\rho_{average} = 0.35$), with $D = E_s h^3 / (12(1 - \nu_s^2))$

h/a	Type	Pattern A			Pattern B			Isotropic plate	
		A1	A2	A3	B1	B2	B3	35% weight	100% weight
SSSS									
0.01	P	2.9084	2.6902	2.2201	1.8869	1.3170	1.3061	9.4755	0.4064 (IGA)
	G	3.1701	2.9055	2.2970	2.1466	1.4597	1.4045		0.4064 [57]
	IWP	2.7541	2.4877	2.0396	1.9172	1.3330	1.3078		0.4064 [56]
	FGPP	2.1041	1.9567	1.6354	1.5306	1.1738	1.1642		
0.1	P	3.0073	2.7951	2.3323	2.0033	1.4472	1.4265	9.5347	0.4272 (IGA)
	G	3.3026	3.0475	2.4519	2.3086	1.6469	1.5763		0.4273 [57]
	IWP	2.8993	2.6396	2.2043	2.0906	1.5268	1.4880		0.4273 [56]
	FGPP	2.1974	2.0572	1.7418	1.6394	1.2962	1.2776		
CCCC									
0.01	P	1.0462	0.9751	0.8022	0.6430	0.4341	0.4288	2.9516	0.1268 (IGA)
	G	1.0260	0.9326	0.7368	0.6972	0.4680	0.4476		0.1268 [57]
	IWP	0.8247	0.7482	0.6161	0.5747	0.4040	0.3987		0.1267 [56]
	FGPP	0.6561	0.6102	0.5102	0.4776	0.3666	0.3635		
0.1	P	1.1603	1.0944	0.9280	0.7696	0.5692	0.5536	3.0176	0.1485 (IGA)
	G	1.1688	1.0833	0.8988	0.8674	0.6583	0.6222		0.1504 [57]
	IWP	0.9740	0.9038	0.7833	0.7497	0.5966	0.5787		0.1499 [56]
	FGPP	0.7544	0.7153	0.6204	0.5901	0.4912	0.4793		

Additionally, the porous plates in this study consist of combinations of six aforementioned density distribution cases and three investigating TPMSs, namely Primitive, Gyroid, and IWP along with the Hashin-Shtrikman-like structure. Various thickness-to-length ratios have been adopted to explore the influence of both flexural and shear stiffness of TPMS on functionally graded plates. From applying the fitting results in the previous section, the mechanical properties including effective elastic modulus, effective shear modulus, and Poisson's ratio of these TPMS structures with a relative density similar to that from other porous cases can be achieved (please see Table. 8). At the relative density of 35%, IWP and Primitive might produce the highest elastic modulus and shear modulus values, respectively. For this reason, P-type plates have the best performance when their thicknesses reach a noticeable value. On the other hand, IWP should be considered a superior structure for thin plate applications. In the case of the Gyroid, a medium value of shear modulus can be found, however, its elastic modulus is only slightly higher than the lowest one. As the result, Gyroid plates' efficiencies might not exceed other TPMS plates with the porous cases in this study. Furthermore, the insignificant differences in Poisson's ratio of all three TPMSs might be negligible due to the minor impact of this property on the bending stiffness of the FG-TPMS plates in Eq. (20). These conclusions can be obtained from the static investigation of uniform porous plates considering core design in Fig. 13.

Nevertheless, these TPMS plates' performances can be modified by employing functional gradations. As a result, thicker zones of TPMS shells can be developed without increasing the average relative density. Therefore, the overall stiffness of the plates might increase. Generally, pattern B should be noted as an improved distribution because it provides two regions for higher relative density at the top and bottom surfaces of the plate, which cannot be found in pattern A. This confirmation can be obtained from both static and buckling analysis results.

Table 7: The non-dimensional buckling load ($\bar{P} = P_{cr}b^2/(\pi^2D)$) along the x direction for rectangular FG plates with various density distribution cases ($h/b = 0.05$, $\rho_{average} = 0.35$)

a/b	Type	Pattern A			Pattern B			Isotropic plate	
		A1	A2	A3	B1	B2	B3	35% weight	100% weight
SSSS									
0.5	P	0.7744	0.8270	0.9953	1.2189	1.7457	1.7721	0.2668	6.0382 (IGA)
	G	0.7598	0.8298	1.0380	1.0965	1.5749	1.6490		5.9873 [59]
	IWP	0.9147	1.004	1.2056	1.2813	1.7681	1.8036		6.0372 [58]
	FGPP	1.1715	1.2540	1.4870	1.5827	2.0204	2.0459		
1	P	0.5512	0.5949	0.7187	0.8451	1.2005	1.2127	0.1712	3.9447 (IGA)
	G	0.5064	0.5517	0.6944	0.7413	1.0759	1.1201		3.9412 [59]
	IWP	0.5825	0.6435	0.7807	0.8287	1.1748	1.1996		3.9444 [58]
	FGPP	0.7633	0.8193	0.9768	1.0420	1.3471	1.3607		
2	P	0.5512	0.5949	0.7187	0.8451	1.2005	1.2128	0.1712	3.9448 (IGA)
	G	0.5064	0.5517	0.6945	0.7413	1.0759	1.1201		3.9811 [59]
	IWP	0.5826	0.6435	0.7808	0.8287	1.1748	1.1996		3.9444 [58]
	FGPP	0.7634	0.8194	0.9768	1.0421	1.3472	1.3607		
CCCC									
0.5	P	2.0499	2.1697	2.5854	3.2421	4.5462	4.6641	0.8171	17.2549 (IGA)
	G	2.1472	2.3362	2.8527	2.9586	4.0257	4.2562		17.2222 [58]
	IWP	2.6716	2.8893	3.3670	3.5458	4.5486	4.6671		
	FGPP	3.3804	3.5822	4.1673	4.3984	5.3795	5.4940		
1	P	1.1831	1.2640	1.5207	1.8760	2.6911	2.7401	0.4293	9.5851 (IGA)
	G	1.1955	1.3069	1.6271	1.7078	2.4310	2.5535		9.5412 [59]
	IWP	1.4690	1.6071	1.9173	2.0363	2.7629	2.8185		9.5588 [58]
	FGPP	1.8634	1.9908	2.3517	2.4984	3.1614	3.2070		
2	P	0.9588	1.0276	1.2356	1.5015	2.1407	2.1769	0.3358	7.5154 (IGA)
	G	0.9450	1.0322	1.2858	1.3527	1.9257	2.0195		7.487 [58]
	IWP	1.1420	1.2520	1.4967	1.5870	2.1669	2.2119		
	FGPP	1.4607	1.5619	1.8463	1.9613	2.4871	2.5219		

Table 8: Mechanical properties of three considering TPMS structures with the relative density of 35%.

Mechanical property	TPMS		
	Primitive	Gyroid	IWP
Effective elastic modulus, E^*	0.122	0.128	0.165
Effective shear modulus, G^*	0.204	0.154	0.137
Poisson's ratio, ν	0.340	0.322	0.271

With low relative density, the elastic modulus of the Gyroid is higher than that of the Primitive. This can be explained by the C_1 value in the fitting curve. However, as in previous statements, the shear response of the Primitive structure is more robust than other types. Consequently, the bending stiffness of P-type plates might outperform the G-type ones in almost all cases. A special case that can be indicated is clamped rectangular plate with distribution pattern A, where the Primitive plates have greater deflections and lower buckling load than the Gyroid ones. Similar results can be found in uniform TPMS plates' responses in Fig. 13 where the relative density ranges from 0.15 to 0.35. Nonetheless, with pattern B, where the lower porosity region of TPMS structures could be better exploited, the higher order deformation mode of Gyroid ($n_2 = 2.351 > 2$) may cause its flexural performance much lesser than others. This distinct behavior of

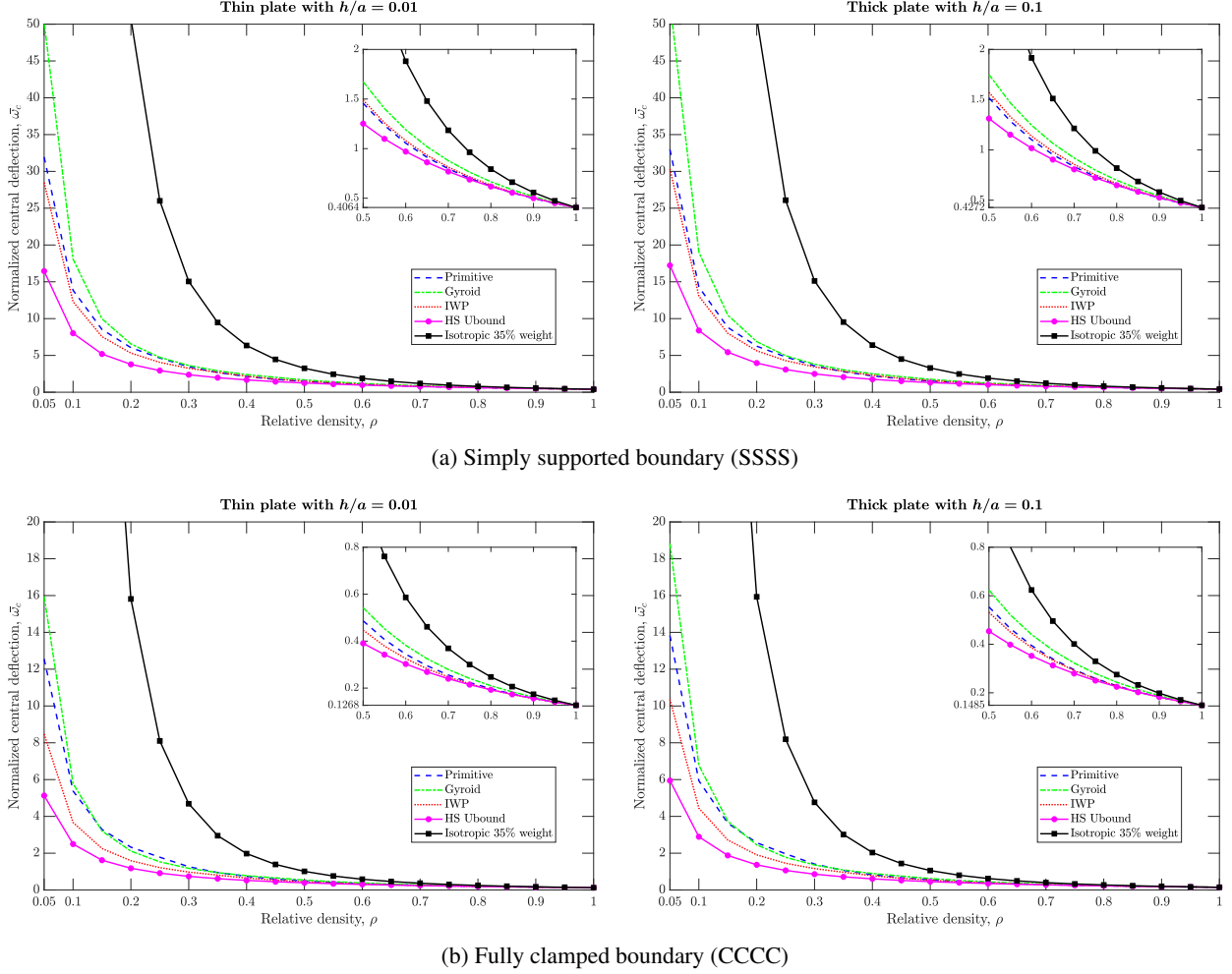


Figure 13: Normalized central deflection \bar{w}_c of square plates with various core designs.

the Gyroid structure should be noticed attentively when utilizing the TPMS structures in applications that require a certain value of porosity.

Although the IWP structure could provide the highest elastic modulus of all three TPMSs, its uniform plate deflection might be slightly larger than the P-based plate ones due to the influence of high shear modulus with considerable relative density, especially in simply supported boundary conditions. In fact, in high relative density ($\rho > 0.6$), Primitive's shear modulus can be greater than the shear modulus of the HS upper boundary [47]. Consequently, porosity distribution B can generate greater stiffness for Primitive FG-TPMS plates in SSSS schemes compared to IWP ones in both static and buckling analysis. In the case of clamped plates, the IWP structures have the best performance in both uniform and non-uniform cases. However, since the relative density reaches 0.75 in the thin plate case and 0.65 in the thick plate case, the static responses of Primitive and IWP applications might approach the same value (please see Fig. 13). Combining the two comments above, for clamped boundary conditions, the P-core thick FG plates with pattern B distribution can have the minimum deflections instead of IWP core ones as the thin FG plates and uniform plates. These values can be seen in Tab. 6.

In buckling load analysis, the results of P-based and IWP-based plates are similar to the static results. For instance, pattern-A plates with IWP cores can produce higher buckling loads than that of the Primitive structures in both boundary conditions. To provide the view of the plate thickness influence, it is observed that for the cases $a/b = 1$ and $a/b = 2$, the minimum thickness-to-length ratio is constantly 0.05 while the value of 0.1 can be observed in the case $a/b = 0.5$. Therefore, this case can be considered a thick-plate case while the rest of the cases are thin-plate cases. The agreement between the response of the thin plate structure in buckling load and that in static load might be achieved with the pattern-B application. However, thick plate responses might be strongly different, where the stiffness of P-core plates

cannot surpass the IWP ones with both simply supported and clamped boundaries. This indicates that the influence of shear modulus in these cases has been reduced. This dissimilarity may come from the plate's aspect ratio and loading direction.

Interestingly, the P-type FG plate behaviors can closely reach the impractical HS porous plate behaviors in all cases. Distribution case B3 provides the lowest disparity among them, which is approximately 10.9% and 12.2% for static and buckling analysis, respectively. However, it is noted that all three TPMS structures investigated in this study could not exceed the HS upper boundary for elastic modulus [47]. Consequently, both two loading schemes of the FG-TPMS plates' responses in this section might be poorer than the boundary despite any relative density distribution. Furthermore, both boundary conditions and thickness of the plate can influence the correlation of FG-TPMS and isotropic plate behaviors. Evidently, the clamped thick plates of Primitive-based structure could only produce 87% and 85% of the HS-based plates' stiffness under static and buckling load, respectively.

To demonstrate the superiority of the FG-TPMS plate, a similar-weight isotropic plate with 35% weight has been investigated by reducing the applied thickness ($h_{applied} = 0.35h$). The plate performances are normalized by the same value as other cases (with the same value of h). The results from Table. 6 and Table. 7 show that the 35% weight isotropic plate could only provide about 1/22 the stiffness of full-weight isotropic plates for both static and buckling responses. This factor might derive from the bending stiffness (D), which is a cubic function of the thickness (h), whereas $(1/0.35)^3 = 1/23.3 \approx 1/22$. In addition, the minimum deflection of all considering six cases is about 3.33 times the value of isotropic plates. This indicates that the flexural behaviors of these plates are approximately 30% the isotropic one. A similar value could also be found in non-dimensional buckling load. In other words, the FG-TPMS plate can generate an approximately seven-times-higher flexural stiffness than that of the weight-reduced isotropic plates. A detailed comparison of the maximum stiffness of all FG-TPMS plates is given in Table. 9. However, it should be noted that the smallest correlation values were obtained from the clamped thick plate cases i.e. 5.45 and 5.71 for static and buckling responses, respectively.

Table 9: Average performance comparisons of FG-TPMS plates with isotropic plates in various analysis types.

Comparison case	Analysis type			
	Rectangular plate			Circular plate
	Static stiffness	Uniaxial buckling load	Free vibration frequency	Free vibration frequency
FG-TPMS to 35% weight isotropic	6.70	6.63	1.60	2.53
FG-TPMS to 100% weight isotropic	0.30	0.30	0.96	0.92
100% weight isotropic to 35% weight isotropic	22.31	22.42	1.67	2.74

Furthermore, there might be an outstanding distribution case that can allow the FG-TPMS plate behaviors to exceed the HS upper boundary regarding stiffness. On the other hand, there were only three types of TPMS structures that have been reviewed in the present study. Numerous other types, that might or might not be micro-mechanically reviewed, can be valuable choices to apply in this porous plate structure. Additionally, the hybridization approach should be considered another dominant solution due to the fact that each TPMS might have a specific strength and weakness. For example, the IWP plates have a remarkable bending modulus while the Primitive can generate the highest shear modulus at high relative density. However, the finding of these cases was not covered due to the scope of this study, yet could be considered for future research in this field.

4.2 Free vibration analysis

In this subsection, the six lowest frequencies of square and circular isotropic plates have been generated by the isogeometric method. Table 10 shows that the results of square plates show a superior agreement with analytical solutions in [60] and [61] for both SSSS and CCCC boundaries, respectively. Moreover, the solutions from the ES-FEM approach have also been adopted for comparison. For circular plates, the solutions of Irie *et al.* [62] are included in Fig. 14 to specify the robustness of the present method. It can be observed that the IGA deviations are much smaller than the ES-FEM ones in most cases. Similar to the previous analysis, one exceptional case is for the fully clamped rectangular

plate with a high thickness-to-length ratio ($h/a = 0.1$). However, it is suggested that the second and third frequencies provided by the IGA method are similar to each other, which is consistent with analytical results. Furthermore, the agreement between analytical and IGA results can also be seen in circular plates with various combinations of thickness-to-radius ratios and boundary conditions.

Table 10: The first six natural frequencies ($\bar{\omega} = (\omega^2 \rho_s a^4 h/D)^{1/4}$) for a square isotropic plate

h/a	Method	Mode					
		1	2	3	4	5	6
SSSS							
0.005	IGA	4.4427	7.0242	7.0242	8.8843	9.9341	9.9341
	ES-FEM [59]	4.4537	7.0565	7.0729	8.9731	10.0410	10.0422
	Ref [60]	4.443	7.025	7.025	8.886	9.935	9.935
0.1	IGA	4.3666	6.7454	6.7454	8.3568	9.2269	9.2269
	ES-FEM [59]	4.3759	6.7692	6.7834	8.4173	9.2968	9.2976
	Ref [60]	4.37	6.74	6.74	8.35	9.22	9.22
CCCC							
0.005	IGA	5.9981	8.5657	8.5657	10.4005	11.4706	11.4978
	ES-FEM [59]	6.0158	8.6075	8.6353	10.5252	11.6032	11.6293
	Ref [61]	5.999	8.568	8.568	10.407	11.472	11.498
0.1	IGA	5.7198	7.9181	7.9181	9.3911	10.2067	10.2494
	ES-FEM [59]	5.7141	7.8990	7.9206	9.3896	10.1935	10.2411
	Ref [61]	5.71	7.88	7.88	9.33	10.13	10.18

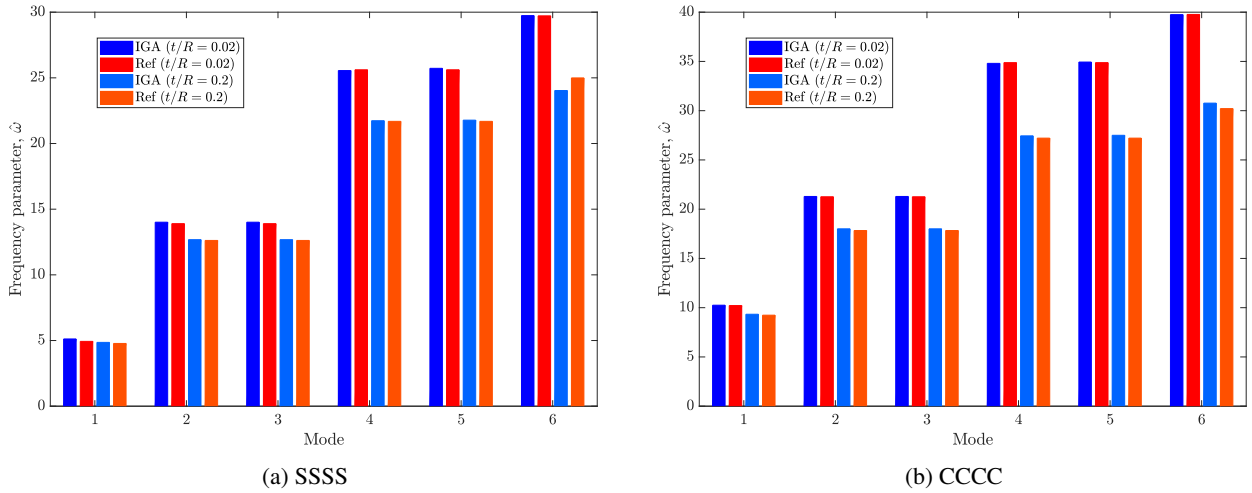


Figure 14: The first six natural frequencies ($\hat{\omega} = \omega R^2 \sqrt{\rho_s h/D}$) of the circular isotropic plate, with $D = E_s h^3 / (12(1 - \nu_s^2))$

Furthermore, the non-dimensional frequencies of constituent functionally graded porous plates are provided in Table. 11 and Table. 12 for square shape and circle shape plates, respectively.

As a result, the free vibration responses of square plates coincide with the static ones. For instance, the Gyroid plates might have the lowest vibration stiffness among others in almost all cases except for clamped pattern-A structures. Both Primitive and IWP plates provide similar stiffness tendencies to the previous section 4.1. However, an unusual case should be noted for the simply supported thin plate with pattern B3. This distribution case with a higher value of power n might produce a larger zone with low relative density in the plate thickness direction. From Fig. 2, the

Table 11: The fundamental frequency parameter ($\bar{\omega} = (\omega^2 \rho_s a^4 h / D)^{1/4}$) for square FG plates with various density distribution cases ($\rho_{average} = 0.35$)

h/a	Type	Pattern A			Pattern B			Isotropic plate with 35% weight
		A1	A2	A3	B1	B2	B3	
SSSS								
0.005	P	3.5274	3.5965	3.7735	3.9322	4.3050	4.3148	2.6284
	G	3.4553	3.5317	3.7455	3.8090	4.1968	4.2384	
	IWP	3.5811	3.6733	3.8603	3.9206	4.2951	4.3161	
	FGPP	3.8292	3.8994	4.0783	4.1463	4.4325	4.4424	
0.1	P	3.4826	3.5452	3.7065	3.8517	4.1759	4.1928	2.6226
	G	3.4047	3.4726	3.6638	3.7183	4.0429	4.0891	
	IWP	3.5188	3.6009	3.7639	3.8131	4.1210	4.1490	
	FGPP	3.7708	3.8325	3.9926	4.0519	4.2939	4.3110	
CCCC								
0.005	P	4.5914	4.6724	4.9064	5.1894	5.7319	5.7507	3.5490
	G	4.6208	4.7332	5.0212	5.0902	5.6285	5.6928	
	IWP	4.8852	5.0055	5.2551	5.3478	5.8442	5.8634	
	FGPP	5.1699	5.2647	5.5060	5.5977	5.9838	5.9971	
0.1	P	4.4454	4.5076	4.6924	4.9193	5.2988	5.3386	3.5253
	G	4.4413	4.5241	4.7343	4.7741	5.1064	5.1814	
	IWP	4.6490	4.7339	4.8999	4.9511	5.2322	5.2746	
	FGPP	4.9562	5.0202	5.1965	5.2588	5.4982	5.5347	

minimum density value was adopted from $-h/4$ to $h/4$ when $n = 3 \div 5$, while a half smaller range was found when $n = 2$. In addition, the thickness-to-length ratio of thin rectangular plates in the previous section is twice the ratio from this section. By combining these contributions, the enhancement of the Primitive shear modulus to plate stiffness might be slightly reduced. However, the deviation between the P-based and IWP-based plates in this application is only about 0.03% and therefore can be negligible. Due to this inconsistency, the best performance density distribution might be influenced by the plate thickness and the analysis types. In other words, the most valuable functional gradation design should be evaluated meticulously.

Moreover, not only the aspect ratio, the plate geometry might give a strong impact on the FG-TPMS behaviors. With an even greater thickness and high relative density zone, the Primitive plates cannot exceed the IWP one in simply supported circular schemes. Besides, the value of disparity between the best-performance FG-TPMS plates and FGPP plates in case B3 is 2.8% typically for square plates while a value of 5.2% is obtained for circular plates. On the other hand, these deviations can indicate that the porous TPMS plates might provide robust imitation to the Hashin-Shtrikman in free vibration responses.

Similar to the previous section, a 35% weight isotropic plate is adopted with the same normalized value as other plates for comparison. The results show that these plates can only produce about $1/1.60 = 62.4\%$ and $1/2.53 = 39.5\%$ the maximum stiffness of TPMS rectangular and circular plates in all distribution cases, respectively. In other words, a higher stiffness can be produced by the FG-TPMS plate with a similar weight. This can be the result of the increment in plate thickness. These thicknesses are $1/0.35 = 2.857$ times larger than the one of 35% weight isotropic plate. Therefore, the greater flexural and shear stiffness could contribute to the overall performance. Furthermore, the highest frequency value of all six cases, which belongs to case B3, can closely reach the value of the 100% weight isotropic plate's one with 96% and 92%, respectively, for the rectangular and circular plates. Consequently, the FG-TPMS plates have proven their superior robustness in vibration application compared to static and buckling cases.

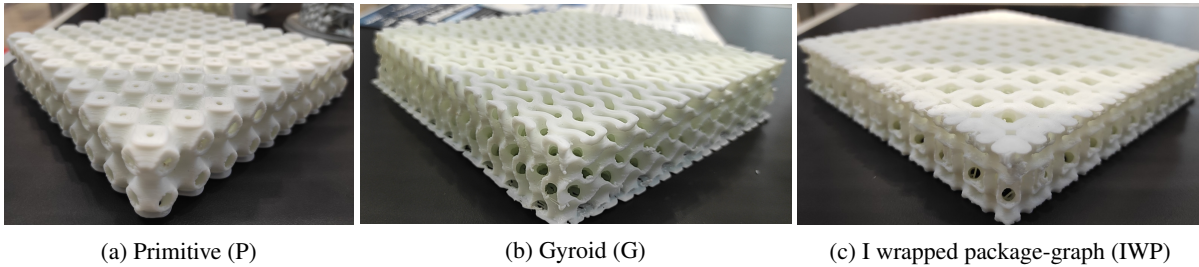
Although the above robustness can also be found in the HS plates with slightly higher values in all cases, there might be only a few realistic materials that give the behavior of the HS upper boundary. Therefore, the HS plate is considered an impractical structure. In contrast, FG-TPMS structures could be fabricated simply by the advances in additive manufacturing (AM) despite any porosity distribution. Numerous studies have verified the mechanical behaviors of metallic TPMS structures that were manufactured by the laser powder bed fusion (LPBF) process. The experimental

Table 12: The fundamental frequency parameter ($\hat{\omega} = \omega R^2 \sqrt{\rho_s h/D}$) for circular FG plates with various density distribution cases ($\rho_{average} = 0.35$)

h/R	Type	Pattern A			Pattern B			Isotropic plate with 35% weight
		A1	A2	A3	B1	B2	B3	
SSSS								
0.02	P	2.9576	3.0848	3.3705	3.7597	4.5789	4.6192	1.8762
	G	3.0467	3.2259	3.6042	3.6432	4.4228	4.5387	
	IWP	3.4057	3.5989	3.9439	4.0402	4.7981	4.8363	
	FGPP	3.7645	3.9220	4.2748	4.3846	5.0041	5.0384	
0.2	P	2.7985	2.9012	3.1623	3.5466	4.2655	4.3139	1.7599
	G	2.8952	3.0474	3.3840	3.4249	4.0770	4.1928	
	IWP	3.2299	3.3913	3.6881	3.7749	4.3849	4.4348	
	FGPP	3.5773	3.7109	4.0258	4.1277	4.6491	4.6935	
CCCC								
0.02	P	6.0679	6.2887	6.9333	7.7165	9.3878	9.4479	3.5917
	G	6.0993	6.3954	7.1948	7.3990	9.0321	9.2369	
	IWP	6.7852	7.1244	7.8522	8.1265	9.7022	9.7709	
	FGPP	7.6174	7.8984	8.6375	8.9267	10.1956	10.2422	
0.2	P	5.7100	5.8759	6.3677	6.9584	8.0363	8.1569	3.5461
	G	5.6468	5.8537	6.4066	6.5218	7.4325	7.6508	
	IWP	6.1469	6.3731	6.8237	6.9595	7.7543	7.8888	
	FGPP	7.0098	7.1906	7.7011	7.8853	8.6064	8.7243	

specimens showed that 3D printing technology could provide high precision for the products fabricated on the digital models, even with complicated functionally graded and hybridization methods [21].

Furthermore, plastic printing is suggested as an arising research area, which is more economical than a metal one. In fact, numerous plastic printing technologies have been used to manufacture complex bio-inspired structures namely material extrusion, material jetting, and VAT polymerization [63]. Fused Deposition modelling (FDM), an AM method of material extrusion technology, can be considered a common method to create TPMS structures with thermal plastic material. Due to the limitation of the printing equipment, the 3D prototypes of the proposed FG-TPMS plates were fabricated with PLA plastic instead of metallic materials. These products can be found in Fig. 15 where the skin layers could be attached afterward. Also, the metallic ones are in progress. However, it is noteworthy that the bulk modulus and the shear modulus of these plastic TPMS might be slightly different from the results of this study due to the inconsistency in the Poisson's ratio of the base materials. Nonetheless, the proposed fitting approach is universally applicable in investigating TPMS structures despite any type of material because of the coincidence of the mechanical response tendencies [3].

Figure 15: The plastic 3D printed versions of FG-TPMS plates with density pattern A and the power $n = 3$.

Therefore, these printed FG-TPMS plates have validated the robustness of additive manufacturing while other traditional fabrication methods might not feasibly create the complicated geometry of TPMSs. Although the presented FG-TPMS

plates in Fig. 15 are made of PLA plastic with the FDM printing method, the metallic printing process of these structures is straightforward with the LPBF technique. With high-tech equipment in printing metal, complex geometry structures such as TPMSs can be fabricated more accurately than plastic ones. For the functional gradation through the thickness of the FG-TPMS plate, plastic printing might not provide sufficient granularity to the product, where a high-order relative density distribution function can be adopted (high value of the power n). In contrast, with the advances in the LPBF method, the resolution of the printing product can be as small as a few dozen of micrometers. However, each method might produce different beneficial and undesirable features for the products. For instance, the filament direction might create a large impact on the performance of specimens in FDM printing. The LPBF printing, however, might consist of multiple micro-porosity which can be created from the chemical composition of the binder. To eliminate these defects in the printing product, the post-processing should be included, namely the heat treatment process for Selective Laser Sintering (SLS) [64].

5 Conclusions

In this study, a new functionally graded TPMS plate model was proposed. Three TPMS architectures including Primitive (P), Gyroid (G), and wrapped package-graph (IWP) with different graded functions were considered. Their effective properties were derived from a new fitting technique based on a two-phase function in terms of relative density. This technique is inspired by the fact that sheet-based TPMS structures' responses strongly depend on their relative density or their thickness. Also, in smaller values of the relative density, these complex geometries have been well-known as stretching-dominated structures. On the other hand, a combining mode of stretching and bending, or even higher-order behaviors, should be noted in heavy foam TPMS structures. By applying the fitting process for the effective moduli, the above conclusion could be observed explicitly in the function parameters. The findings were obtained and further utilized to estimate Poisson's ratios for each TPMS type. Then, a seventh-order shear deformation theory (SeSDT) was investigated to describe the generalized displacement field of the FG-TPMS plate. A modification in the constitutive matrix has been conducted to capture the cubic symmetrical behavior of TPMS structures. NURBS-based isogeometric analysis (IGA) was employed to fulfill the C^1 continuity in approximations. Static, buckling, and free vibration analyses of rectangular and circular FG-TPMS plates were illustrated. Some concluding remarks can be coined as

- A two-phase fitting function in terms of the relative density produced ultra-accurate results in comparison with the previously published results.
- The obtained solutions from the present approach show good agreement with the results of analytical theories and other numerical methods.
- The FG-TPMS plate model exhibited an excellent alternative for the isotropic plate. With only 35% weight, the FG-TPMS plate is still able to mimic the fundamental frequency of the 100% weight isotropic one.
- It was observed that the constituent structures provide dominant responses compared with similar-weight isotropic plates (0.35-thickness plates). The approximately three times higher and seven times higher values could be indicated from the previous section's results for fundamental frequency and both non-dimensional buckling and static load, respectively.
- Another major aspect of the FG-TPMS plates is their ability to be fabricated with multiple scales from macroscale to nanoscale with various manufacturing approaches. Among all, 3D printing technology might be the most feasible one with rapid developments in both macroscale and microscale printing.

As demonstrated in the previous section, additive manufacturing should be indicated as a suitable approach to fabricating sophisticated TPMS structures. Thanks to the advances in 3D printing technology, various types of materials may be adopted for the TPMS porous plates taken into account metal, plastic, ceramic, fibre-reinforced concrete, and other existing ones. Although this manufacturing technology might remain several limitations such as nanoscale printing ability, micro-deflections, etc. Numerous solutions have been introduced and are continuously investigated to improve the technology. In sum, by adopting AM process, these FG-TPMS structures could expand numerous new potential application features in the future.

Acknowledgements

This research used resources of the high-performance computer cluster (HPCC) at the Advanced Institute of Materials Science, Ton Duc Thang University (TDTU).

References

- [1] Ngoc San Ha and Guoxing Lu. A review of recent research on bio-inspired structures and materials for energy absorption applications. *Composites Part B*, 181:107496, 2020. doi:10.1016/j.compositesb.2019.107496.
- [2] Diab W. Abueidda, Rashid K. Abu Al-Rub, Ahmed S. Dalaq, Dong-Wook Lee, Kamran A. Khan, and Iwona Jasiuk. Effective conductivities and elastic moduli of novel foams with triply periodic minimal surfaces. *Mechanics of Materials*, 95:102–115, 2016. ISSN 0167-6636. doi:10.1016/j.mechmat.2016.01.004.
- [3] Oraib Al-Ketan and Rashid K. Abu Al-Rub. Multifunctional mechanical metamaterials based on triply periodic minimal surface lattices. *Advanced Engineering Materials*, 21(10):1900524, 2019. ISSN 1438-1656. doi:doi.org/10.1002/adem.201900524.
- [4] M.M. Sychov, L.A. Lebedev, S.V. Dyachenko, and L.A. Nefedova. Mechanical properties of energy-absorbing structures with triply periodic minimal surface topology. *Acta Astronautica*, 150:81–84, 2018. ISSN 0094-5765. doi:10.1016/j.actaastro.2017.12.034.
- [5] Lei Zhang, Stefanie Feih, Stephen Daynes, Shuai Chang, Michael Yu Wang, Jun Wei, and Wen Feng Lu. Energy absorption characteristics of metallic triply periodic minimal surface sheet structures under compressive loading. *Additive Manufacturing*, 23:505–515, 2018. ISSN 2214-8604. doi:doi.org/10.1016/j.addma.2018.08.007.
- [6] Yingjing Liang, Wei Zhou, Yijie Liu, Zhanshuo Li, Yang Yang, Huifeng Xi, and Zhigang Wu. Energy absorption and deformation behavior of 3d printed triply periodic minimal surface stainless steel cellular structures under compression. *steel research international*, 92(3), 2020. ISSN 1611-3683 1869-344X. doi:10.1002/srin.202000411.
- [7] Wenjing Yang, Jia An, Kai Chua, and Kun Zhou. Acoustic absorptions of multifunctional polymeric cellular structures based on triply periodic minimal surfaces fabricated by stereolithography. *Virtual and Physical Prototyping*, 15:1–8, 03 2020. doi:10.1080/17452759.2020.1740747.
- [8] Chunguan Lin, Guilin Wen, Hanfeng Yin, Zhen-Pei Wang, Jie Liu, and Yi Min Xie. Revealing the sound insulation capacities of tpms sandwich panels. *Journal of Sound and Vibration*, 540, 2022. ISSN 0022460X. doi:10.1016/j.jsv.2022.117303.
- [9] Liya Zhu, Lan Li, Zong-an Li, Jian-ping Shi, Wen-lai Tang, Ji-quan Yang, and Phoenix Zhang. Design and biomechanical characteristics of porous meniscal implant structures using triply periodic minimal surfaces. *Journal of Translational Medicine*, 17, 03 2019. doi:10.1186/s12967-019-1834-2.
- [10] Teerapong Poltue, Chatchai Karuna, Suppakrit Khrueduangkham, Saran Seehanam, and Patcharapit Promoppatum. Design exploration of 3d-printed triply periodic minimal surface scaffolds for bone implants. *International Journal of Mechanical Sciences*, 211, 2021. ISSN 00207403. doi:10.1016/j.ijmecsci.2021.106762.
- [11] Phuong Tran and Chenxi Peng. Triply periodic minimal surfaces sandwich structures subjected to shock impact. *Journal of Sandwich Structures & Materials*, 23(6):2146–2175, 2020. ISSN 1099-6362 1530-7972. doi:doi.org/10.1177/1099636220905551.
- [12] Chenxi Peng, Kate Fox, Ma Qian, H. Nguyen-Xuan, and Phuong Tran. 3d printed sandwich beams with bioinspired cores: Mechanical performance and modelling. *Thin-Walled Structures*, 161, 2021. ISSN 02638231. doi:doi.org/10.1016/j.tws.2021.107471.
- [13] V. Nguyen-Van, NK. Choudhry, B. Panda, and Phuong Tran H. Nguyen-Xuan. Performance of concrete beam reinforced with 3d printed bioinspired primitive scaffold subjected to three-point bending. *Automation in Construction*, 134:104060, 2022. doi:10.1016/j.autcon.2021.104060.
- [14] Vuong Nguyen-Van, Junli Liu, Chenxi Peng, Guomin Zhang, H. Nguyen-Xuan, and Phuong Tran. Dynamic responses of bioinspired plastic-reinforced cementitious beams. *Cement and Concrete Composites*, 133:104682, 2022. ISSN 0958-9465. doi:doi.org/10.1016/j.cemconcomp.2022.104682.
- [15] Bao-Loi Dang, Vuong Nguyen-Van, Phuong Tran, Magd Abdel Wahab, Klaus Hackl, and H. Nguyen-Xuan. Mechanical and hydrodynamic characteristics of emerged porous gyroid breakwaters based on triply periodic minimal surfaces. *Ocean Engineering*, 254:111392, 2022. doi:10.1016/j.oceaneng.2022.111392.
- [16] Chatchai Karuna, Teerapong Poltue, Suppakrit Khrueduangkham, and Patcharapit Promoppatum. Mechanical and fluid characteristics of triply periodic minimal surface bone scaffolds under various functionally graded strategies. *Journal of Computational Design and Engineering*, 9(4):1258–1278, 2022. ISSN 2288-5048. doi:10.1093/jcde/qwac052.
- [17] Junjian Fu, Pengfei Sun, Yixian Du, Hao Li, Xiangman Zhou, and Qihua Tian. Isotropic design and mechanical characterization of tpms-based hollow cellular structures. *Composite Structures*, 279, 2022. ISSN 02638223. doi:10.1016/j.compstruct.2021.114818.

- [18] Komal Chawla and Raj Kiran. Numerical predictions for the effect of negative poisson's ratio on thermoelastic properties of triply periodic minimal surface-based composites. *Results in Materials*, 14, 2022. ISSN 2590048X. doi:10.1016/j.rinma.2022.100273.
- [19] Oraib Al-Ketan. Programmed plastic deformation in mathematically-designed architected cellular materials. *Metals*, 11(10), 2021. ISSN 2075-4701. doi:10.3390/met11101622.
- [20] N.V Viet and W Zaki. Free vibration and buckling characteristics of functionally graded beams with triply periodic minimal surface architecture. *Composite Structures*, 274:114342, 2021. doi:10.1016/j.compstruct.2021.114342.
- [21] Chukwugozie J. Ejeh, Imad Barsoum, and Rashid K. Abu Al-Rub. Flexural properties of functionally graded additively manufactured alsi10mg tpms latticed-beams. *International Journal of Mechanical Sciences*, 223, 2022. ISSN 00207403. doi:10.1016/j.ijmecsci.2022.107293.
- [22] Chenxi Peng and Phuong Tran. Bioinspired functionally graded gyroid sandwich panel subjected to impulsive loadings. *Composites Part B: Engineering*, 188, 2020. ISSN 13598368. doi:doi.org/10.1016/j.compositesb.2020.107773.
- [23] Tuan N. Nguyen, Chien H. Thai, and H. Nguyen-Xuan. On the general framework of high order shear deformation theories for laminated composite plate structures: A novel unified approach. *International Journal of Mechanical Sciences*, 110:242 – 255, 2016. doi:10.1016/j.ijmecsci.2016.01.012.
- [24] Tuan N. Nguyen, Tuan D. Ngo, and H. Nguyen-Xuan. A novel three-variable shear deformation plate formulation: Theory and isogeometric implementation. *Computer Methods in Applied Mechanics and Engineering*, 326:376 – 401, 2017. ISSN 0045-7825. doi:10.1016/j.cma.2017.07.024.
- [25] J. N. Reddy. A Simple Higher-Order Theory for Laminated Composite Plates. *Journal of Applied Mechanics*, 51(4):745–752, 12 1984. ISSN 0021-8936. doi:10.1115/1.3167719.
- [26] Rameshchandra P. Shimpi. Refined plate theory and its variants. *AIAA Journal*, 40(1):137 – 146, 2002. doi:10.2514/2.1622.
- [27] H. Nguyen-Xuan, Chien H. Thai, and T. Nguyen-Thoi. Isogeometric finite element analysis of composite sandwich plates using a higher order shear deformation theory. *Composites Part B: Engineering*, 55:558 – 574, 2013. ISSN 1359-8368. doi:10.1016/j.compositesb.2013.06.044.
- [28] J.L.Mantari, A.S.Oktem, and C. Guedes Soares. A new trigonometric shear deformation theory for isotropic, laminated composite and sandwich plates. *International Journal of Solids and Structures*, 49:43–53, 2012. doi:10.1016/j.ijsolstr.2011.09.008.
- [29] Chien H. Thai, A.J.M. Ferreira, S.P.A. Bordas, T. Rabczuk, and H. Nguyen-Xuan. Isogeometric analysis of laminated composite and sandwich plates using a new inverse trigonometric shear deformation theory. *European Journal of Mechanics - A/Solids*, 43:89 – 108, 2014. ISSN 0997-7538. doi:j.euromechsol.2013.09.001.
- [30] T.J.R. Hughes, J.A. Cottrell, and Y. Bazilevs. Isogeometric analysis: Cad, finite elements, nurbs, exact geometry and mesh refinement. *Computer Methods in Applied Mechanics and Engineering*, 194(39):4135 – 4195, 2005. ISSN 0045-7825. doi:10.1016/j.cma.2004.10.008.
- [31] Chien H. Thai, H. Nguyen-Xuan, N. Nguyen-Thanh, T-H. Le, T. Nguyen-Thoi, and T. Rabczuk. Static, free vibration, and buckling analysis of laminated composite reissner–mindlin plates using nurbs-based isogeometric approach. *International Journal for Numerical Methods in Engineering*, 91(6):571 – 603, 2012. doi:10.1002/nme.4282.
- [32] Yujie Guo and Martin Ruess. A layerwise isogeometric approach for nurbs-derived laminate composite shells. *Composite Structures*, 124:300–309, 2015. doi:j.compstruct.2015.01.012.
- [33] Shirko Faroughi, Erfan Shafei, and Timon Rabczuk. Anisotropic solid-like shells modeled with nurbs-based isogeometric approach: vibration, buckling, and divergence analyses. *Computer Methods in Applied Mechanics and Engineering*, 359:112668, 2020. doi:10.1016/j.cma.2019.112668.
- [34] Jiazhao Huang, Nhon Nguyen-Thanh, Jingwen Gao, Zheng Fan, and Kun Zhou. Static, free vibration, and buckling analyses of laminated composite plates via an isogeometric meshfree collocation approach. *Composite Structures*, 285:115011, 2022. doi:10.1016/j.compstruct.2021.115011.
- [35] Navid Valizadeh, Sundararajan Natarajan, Octavio A. Gonzalez-Estrada, Timon Rabczuk, Tinh Quoc Bui, and Stéphane P.A. Bordas. Nurbs-based finite element analysis of functionally graded plates: Static bending, vibration, buckling and flutter. *Composite Structures*, 99:309 – 326, 2013. doi:10.1016/j.compstruct.2012.11.008.
- [36] Chien H. Thai, S. Kulasegaram, Loc V. Tran, and H. Nguyen-Xuan. Generalized shear deformation theory for functionally graded isotropic and sandwich plates based on isogeometric approach. *Computers Structures*, 141:94 – 112, 2014. ISSN 0045-7949. doi:10.1016/j.compstruc.2014.04.003.

- [37] Hoang X. Nguyen, Tuan N. Nguyen, M. Abdel-Wahab, S.P.A. Bordas, H. Nguyen-Xuan, and Thuc P. Vo. A refined quasi-3d isogeometric analysis for functionally graded microplates based on the modified couple stress theory. *Computer Methods in Applied Mechanics and Engineering*, 313:904 – 940, 2017. ISSN 0045-7825. doi:10.1016/j.cma.2016.10.002.
- [38] Tan N. Nguyen, Chien H. Thai, Anh-Tuan Luu, H. Nguyen-Xuan, and Jaehong Lee. Nurbs-based postbuckling analysis of functionally graded carbon nanotube-reinforced composite shells. *Computer Methods in Applied Mechanics and Engineering*, 347:983–1003, 2019. doi:10.1016/j.cma.2019.01.011.
- [39] Jiankang Zhang, Tiantang Yu, Le Van Lich, and Tinh Quoc Bui. Composite fg plates with different internal cutouts: Adaptive iga buckling analysis without trimmed surfaces. *Composite Structures*, 259:113392, 2021. doi:10.1016/j.compstruct.2020.113392.
- [40] A. Patton, P. Antolín, J. Kiendl, and A. Reali. Efficient equilibrium-based stress recovery for isogeometric laminated curved structures. *Composite Structures*, 272:113975, 2021. doi:10.1016/j.compstruct.2021.113975.
- [41] Joris J.C. Remmers E. Börjesson and Martin Fagerström. An adaptive isogeometric shell element for the prediction of initiation and growth of multiple delaminations in curved composite structures. *Computers and Structures*, 260:106701, 2022. doi:10.1016/j.compstruc.2021.106701.
- [42] C.M. Zener and S. Siegel. Elasticity and anelasticity of metals. *The Journal of Physical and Colloid Chemistry*, 53(9):1468, 1949. doi:10.1021/j150474a017.
- [43] Lorna J. Gibson. Cellular solids. *Mrs Bulletin*, 28(4):270–274, 2003. ISSN 1938-1425.
- [44] Dong-Wook Lee, Kamran A. Khan, and Rashid K. Abu Al-Rub. Stiffness and yield strength of architected foams based on the schwarz primitive triply periodic minimal surface. *International Journal of Plasticity*, 95:1–20, 2017. ISSN 0749-6419. doi:doi.org/10.1016/j.ijplas.2017.03.005.
- [45] N. V. Viet, N. Karathanasopoulos, and W. Zaki. Mechanical attributes and wave propagation characteristics of tpms lattice structures. *Mechanics of Materials*, 172, 2022. ISSN 01676636. doi:10.1016/j.mechmat.2022.104363.
- [46] Ugur Simsek, Aykan Akbulut, Cemal Efe Gayir, Cansu Basaran, and Polat Sendur. Modal characterization of additively manufactured tpms structures: comparison between different modeling methods. *The International Journal of Advanced Manufacturing Technology*, 115(3):657–674, 2020. ISSN 0268-3768 1433-3015. doi:10.1007/s00170-020-06174-0.
- [47] Zeyao Chen, Yi Min Xie, Xian Wu, Zhe Wang, Qing Li, and Shiwei Zhou. On hybrid cellular materials based on triply periodic minimal surfaces with extreme mechanical properties. *Materials & Design*, 183, 2019. ISSN 02641275. doi:10.1016/j.matdes.2019.108109.
- [48] Diab W. Abueidda, Mete Bakir, Rashid K. Abu Al-Rub, Jörgen S. Bergström, Nahil A. Sobh, and Iwona Jasiuk. Mechanical properties of 3d printed polymeric cellular materials with triply periodic minimal surface architectures. *Materials & Design*, 122:255–267, 2017. ISSN 02641275. doi:10.1016/j.matdes.2017.03.018.
- [49] Oraib Al-Ketan, Rachid Rezgui, Reza Rowshan, Huifeng Du, Nicholas X. Fang, and Rashid K. Abu Al-Rub. Microarchitected stretching-dominated mechanical metamaterials with minimal surface topologies. *Advanced Engineering Materials*, 20(9), 2018. ISSN 14381656. doi:10.1002/adem.201800029.
- [50] K. Abu Al-Rub Rashid, Dong-Wook Lee, A. Khan Kamran, and N. Palazotto Anthony. Effective anisotropic elastic and plastic yield properties of periodic foams derived from triply periodic schoen’s i-wp minimal surface. *Journal of Engineering Mechanics*, 146(5):04020030, 2020. doi:10.1061/(ASCE)EM.1943-7889.0001759.
- [51] Oraib Al-Ketan, Rashid K. Abu Al-Rub, and Reza Rowshan. The effect of architecture on the mechanical properties of cellular structures based on the iwp minimal surface. *Journal of Materials Research*, 33(3):343–359, 2018. ISSN 0884-2914 2044-5326. doi:10.1557/jmr.2018.1.
- [52] S. C. Han, J. W. Lee, and K. Kang. A new type of low density material: Shellular. *Adv Mater*, 27(37):5506–11, 2015. ISSN 1521-4095 (Electronic) 0935-9648 (Linking). doi:10.1002/adma.201501546.
- [53] Diab W. Abueidda, Mohamed Elhebeary, Cheng-Shen Shiang, Siyuan Pang, Rashid K. Abu Al-Rub, and Iwona M. Jasiuk. Mechanical properties of 3d printed polymeric gyroid cellular structures: Experimental and finite element study. *Materials & Design*, 165, 2019. ISSN 02641275. doi:10.1016/j.matdes.2019.107597.
- [54] J. Austin Cottrell, Thomas J. R Hughes, and Yuri Bazilevs. *Isogeometric Analysis: Toward Integration of CAD and FEA*. Wiley, A John Wiley and Sons, Ltd, 2009.
- [55] Zvi Hashin and Shmuel Shtrikman. A variational approach to the theory of the elastic behaviour of multiphase materials. *Journal of the Mechanics and Physics of Solids*, 11(2):127–140, 1963. ISSN 0022-5096.

- [56] Robert L. Taylor and Ferdinando Auricchio. Linked interpolation for reissner-mindlin plate elements: Part ii—a simple triangle. *International Journal for Numerical Methods in Engineering*, 36(18):3057–3066, 1993. ISSN 0029-5981. doi:<https://doi.org/10.1002/nme.1620361803>. URL <https://doi.org/10.1002/nme.1620361803>.
- [57] H. Nguyen-Xuan, T. Rabczuk, Stéphane Bordas, and J. F. Debonnie. A smoothed finite element method for plate analysis. *Computer Methods in Applied Mechanics and Engineering*, 197(13-16):1184–1203, 2008. ISSN 00457825. doi:10.1016/j.cma.2007.10.008.
- [58] S. Kitipornchai, Y. Xiang, C. M. Wang, and K. M. Liew. Buckling of thick skew plates. *International Journal for Numerical Methods in Engineering*, 36(8):1299–1310, 1993. ISSN 0029-5981. doi:doi.org/10.1002/nme.1620360804.
- [59] H. Nguyen-Xuan, G. R. Liu, C. Thai-Hoang, and T. Nguyen-Thoi. An edge-based smoothed finite element method (es-fem) with stabilized discrete shear gap technique for analysis of reissner–mindlin plates. *Computer Methods in Applied Mechanics and Engineering*, 199(9-12):471–489, 2010. ISSN 00457825. doi:10.1016/j.cma.2009.09.001.
- [60] F. Abbassian, D. J. Dawswell, N. C. Knowles, and F. Abassian. *Free vibration benchmarks*. NAFEMS, 1987.
- [61] Robert D. Blevins and R. Plunkett. Formulas for natural frequency and mode shape. *Journal of Applied Mechanics*, 47(2):461–462, 1980. ISSN 0021-8936. doi:doi.org/10.1115/1.3153712.
- [62] T. Irie, G. Yamada, and S. Aomura. Natural frequencies of mindlin circular plates. *Journal of Applied Mechanics*, 47(3):652–655, 1980. ISSN 0021-8936. doi:10.1115/1.3153748.
- [63] Shakib Hyder Siddique, Paul J. Hazell, Hongxu Wang, Juan P. Escobedo, and Ali A. H. Ameri. Lessons from nature: 3d printed bio-inspired porous structures for impact energy absorption – a review. *Additive Manufacturing*, 58, 2022. ISSN 22148604. doi:10.1016/j.addma.2022.103051.
- [64] Oraib Al-Ketan, Reza Rowshan, Anthony N. Palazotto, and Rashid K. Abu Al-Rub. On mechanical properties of cellular steel solids with shell-like periodic architectures fabricated by selective laser sintering. *Journal of Engineering Materials and Technology*, 141(2), 2019. ISSN 0094-4289 1528-8889. doi:10.1115/1.4041874.